Nuclear Instruments and Methods in Physics Research A 373 (1996) 227–260

NUCLEAR INSTRUMENTS & METHODS IN PHYSICS RESEARCH Section A

Track finding and fitting in the H1 Forward Track Detector

S. Burke[a,*], R.C.W. Henderson[a], S.J. Maxfield[b], J.V. Morris[c], G.D. Patel[b], D.P.C. Sankey[c], I.O. Skillicorn[d]

[a] *Lancaster University, Lancaster LA1 4YB, UK*
[b] *University of Liverpool, Liverpool L69 3BX, UK*
[c] *Rutherford Appleton Laboratory, Didcot, Oxon., OX11 0QX, UK*
[d] *University of Glasgow, Glasgow G12 8QQ, UK*

Received 30 June 1995

Abstract

The tracking environment in the H1 Forward Track Detector, where the hit multiplicity from proton fragments is high, is particularly hostile. The techniques and software which have been developed for pattern recognition and Kalman fitting of charged particle tracks in this region are described in detail.

1. Introduction

The Forward Track Detector (FTD) is part of the H1 detector used at the HERA accelerator to study high energy electron–proton collisions. This paper describes the software used for the pattern recognition and fitting of tracks measured by the Forward Tracker. To set the framework and to motivate the design of the FTD, Section 1 discusses the HERA accelerator and its physics goals, and outlines the construction of the H1 detector. Section 2 describes the hardware of the FTD. The techniques used to find the hits in the drift chamber data are presented in Section 3, and calibration and monitoring procedures are described in Section 4. Sections 5 and 6 discuss the algorithms developed for finding line segments in the drift chambers and the methods used for joining the segments to form tracks. A Kalman filter technique is used for determining track parameters; this is described in Section 7. The method used to align the Forward Tracker is outlined in Section 8. Details of the performance of the software and the relation between this performance and that of the hardware are given in Section 9. Section 10 summarises the conclusions.

1.1. The HERA accelerator

The HERA accelerator has been constructed to investigate lepton–quark interactions at high energy by colliding 30 GeV electrons with 820 GeV protons. The experimental programme at HERA includes searches for new physics, such as massive new bosons, super-symmetric particles, lepton and quark substructure, and heavy leptons. It permits measurement of the proton structure functions up to values of Q^2 that are two orders of magnitude greater than previous experiments and down to values of x_{Bj} two orders of magnitude lower [1].

1.2. The H1 detector

The kinematics of HERA collisions lead to an asymmetric detector design [2]. The centre of mass of the collision moves in the proton direction, and consequently any collision products are boosted along this direction. The H1 detector is designed to provide a smooth and homogeneous response from small forward angles (with respect to the proton direction) through to backward angles. The measurement of charged tracks at small angles requires a Forward Tracker.

The detector layout is illustrated in Fig. 1. It includes:

- The Central Track Detector (CTD), (1), made up of a central jet chamber (CJC), interleaved with two z-chambers and multi-wire proportional chambers (MWPCs).
- The Forward Track Detector, (2), consisting of three layers of Radial and Planar drift chambers with MWPCs and transition radiators. The FTD is described in greater detail in the following section.
- An electromagnetic calorimeter, (3), with lead plates as the showering material and liquid argon (LAr) as the detector medium in the forward and barrel region, and a lead scintillator sandwich (BEMC), (8), in the backward region.
- An hadronic calorimeter, (4), using LAr with stainless steel absorber plates.

* Corresponding author.

SSDI 0168-9002(95)00692-3

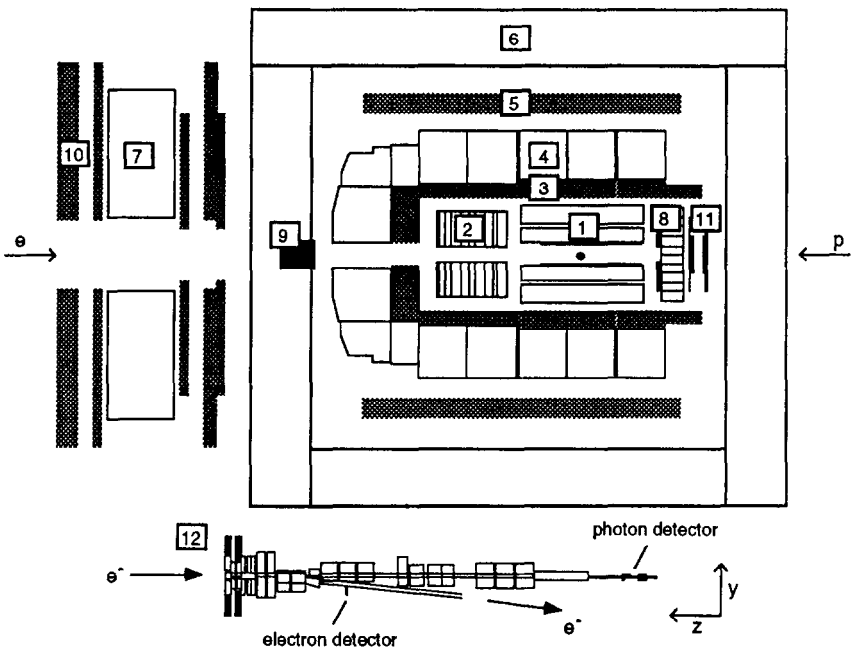

Fig. 1. Schematic y–z view of the H1 detector. Also included is the luminosity monitor, situated downstream in the electron direction (not to scale). The nominal interaction point is marked by •. See text for key.

- A superconducting solenoid giving a field of about 1.2 T, (5), outside the hadronic calorimeter.
- An outer shell of iron plates to contain the return magnetic flux, (6). The iron is interleaved with plastic streamer tubes to act as a tail-catcher for the hadronic calorimeter and as a muon detector and tracker.
- Additional muon detection, provided by three layers of muon chambers in the barrel and forward region, along with a forward muon spectrometer, which consists of a magnetised iron toroid, (7), and six layers of drift chambers, (10).
- A plug calorimeter, (9), to detect hadronic energy at small angles (>0.7°) built as a copper and silicon sandwich.
- A time-of-flight scintillator, (11), to veto events not originating at the vertex.
- A luminosity monitor, (12).

1.2.1. The H1 coordinate system

The H1 coordinate system is right-handed and is defined with respect to the Central Tracker. The nominal positive z-axis is in the proton direction with the y-axis vertical; θ and ϕ represent the polar and azimuthal angles respectively, and in this paper R denotes the radial coordinate in the x, y plane. The origin of the coordinate system is defined to be at the centre of the CTD (the nominal e–p interaction point).

2. Overview of the Forward Track Detector

The H1 Forward Track Detector, shown in Fig. 2, covers the laboratory angles between 5° and 30° with respect to the proton beam direction. The sensitive region of the chambers is the cylindrical volume 134 cm $< z <$ 254 cm, and 15 cm $< R <$ 79 cm. This region is a particularly hostile environment for tracking. The primary track multiplicity, typically low momentum products from fragmentation of the proton, is ~10–15 and is strongly concentrated at small radii. In addition, material in the end wall of the CTD and around the beam pipe produces a large number of secondary tracks. This results in a high hit density with frequent overlapping of hits and loss of information. The problem is exacerbated by the presence of a collimator situated in the beam pipe at z = 204 cm, as shown in Fig. 2, which floods the rear of the Tracker with

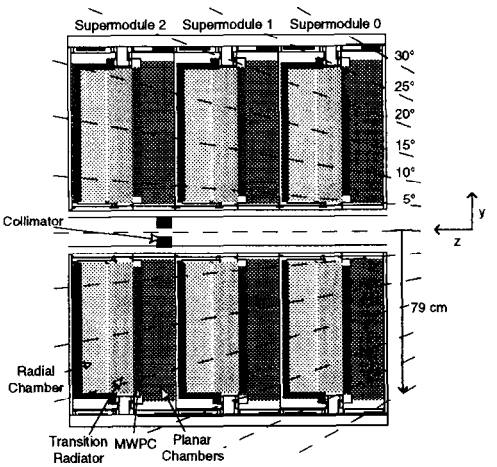

Fig. 2. Schematic view of the H1 Forward Track Detector. The polar angles for tracks from the origin are also indicated.

additional secondary tracks, doubling the number of hits in that region. Consequently 80% of all tracks and 60% of those with momentum, p, >0.5 GeV/c which penetrate the Forward Tracker are secondaries.

The design objectives for the Forward Tracker were [3]:

- momentum resolution for tracks ($p > 10$ GeV/c) constrained to the primary vertex of $\sigma(p)/p^2 \sim 0.003$ (GeV/c)$^{-1}$,
- angular resolution of <1 mrad,
- efficient track pattern recognition,
- efficient electron identification, with pion contamination below 10% for particle momenta up to 60 GeV/c,
- a fast ray trigger (provided by the MWPCs).

The last two points are not discussed in this paper [4]. These objectives were subject to the overall constraint of introducing the minimum amount of material before the calorimeter [5].

The detector is realised as three identical sub-units, known as Supermodules, numbered from 0 to 2 with increasing z. Each Supermodule, when seen from the direction of the incoming proton, consists firstly of three layers of Planar drift chambers, oriented at 0°, +60° and −60° to the vertical, followed by an MWPC, then transition radiator material, and finally a Radial drift chamber. As each part of the Supermodule uses a different gas mixture (Ar/C_3H_8 for the Planar chambers and MWPCs, He/CO_2 for the transition radiator and Ar/C_2H_6 or $Xe/He/C_2H_6$ for the Radial chambers) each Supermodule is housed in a correspondingly segmented gas tank. The tank also forms the mechanical frame for the FTD, supporting it on rails inside the liquid argon cryostat.

2.1. The Radial chambers

Each of the three Radial drift chambers, situated approximately 1.7, 2.1 and 2.5 m from the interaction point, consists of 48 wedge-shaped segments, each segment subtending 7.5° in ϕ [6]. The layout of a Radial chamber is shown in Fig. 3. Each segment contains a plane of twelve sense wires, spaced apart by 1 cm along the beam direction, and eleven intermediate field wires, strung between a central hub and the outer shell. The sense wires are alternately staggered by 288 μm out of the true radial wire-plane, to permit resolution of the left/right track ambiguity.

The radial wire geometry described above was dictated by the following considerations:

- the available space is filled most efficiently, providing drift cells of smaller size at smaller radius, where track illumination is higher;
- multi-track pattern recognition is optimised, because a track makes hits which have a linear dependence of ϕ on z;
- the drift time measurement is an accurate determination of the track sagitta in the R–ϕ plane (orthogonal to the magnetic field), so that optimum particle momentum precision may be achieved.

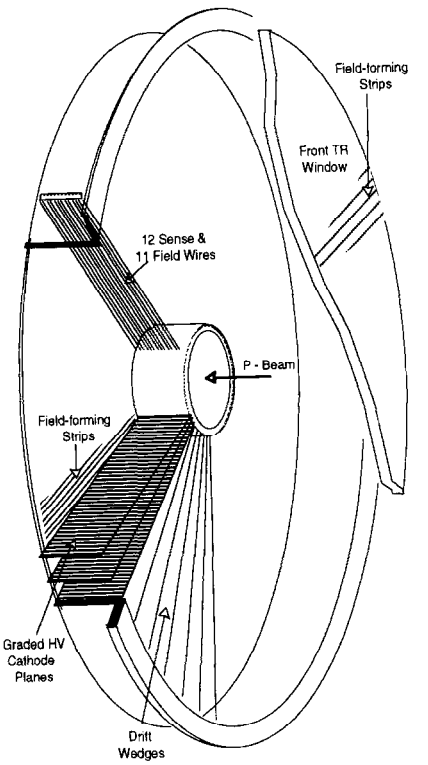

Fig. 3. Perspective schematic of a Radial chamber.

The sense wires are 50 μm diameter Stablohm 800. The simultaneous requirements of having the chamber operate in a proportional mode for energy loss measurements and of demanding total ionisation collection for efficient transition radiation (X-ray) detection dictate the choice of relatively large diameter sense wires. At the hub each sense wire is connected to its partner 105° away in ϕ; each such wire-pair is read out at the outer circumference of the chamber and the radial coordinate reconstructed from charge division along the wire-pair.

2.2. The Planar chambers

The Planar system consists of three identical modules situated approximately 1.4, 1.8, and 2.2 m from the interaction point [2]. Each module consists of 12 planes of wires perpendicular to the z-axis. Each plane contains 32 parallel sense wires of diameter 40 μm with a spacing of 5.7 cm. These wires form a sensitive disc of radius 79 cm perpendicular to the beam direction. There is a concentric 15 cm radius hole in the disc for the beam pipe, and wires that would otherwise cross this are split into two separate parts. Within a module the first four planes have wires which are aligned vertically, the next four at 60° and the final four at −60° to the vertical. These three sets of planes are referred to as the X, U, and V orientations respectively, Fig. 4.

An orientation consists of 32 cells each containing four

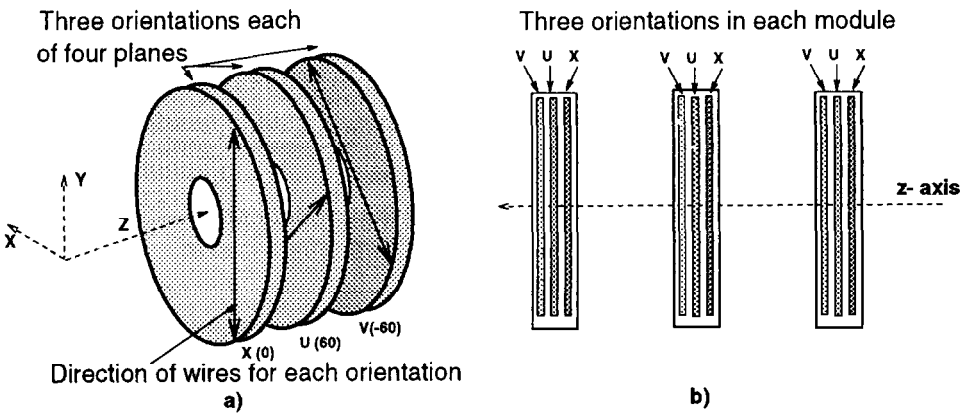

Fig. 4. Details of Planar orientations. (a) A full Planar module comprising three orientations and (b) the configuration of the X, U, V orientations within the Forward Tracker.

sense and ten grid wires. The sense wires are separated by 0.6 cm along the z axis and staggered by 300 μm either side of the cell centre with a maximum drift distance of approximately 2.8 cm, see Fig. 5.

The three orientations of a Planar chamber module allow the reconstruction of a track segment that is well defined in both the radial and ϕ directions and thus the Planar chambers complement the Radial chambers that measure accurately in ϕ only.

3. Hit finding in the drift chambers

The sense wires in the Forward Tracker are read out using 104 MHz 8 bit nonlinear Flash Analogue-to-Digital Converters (FADCs) giving a history of the chamber pulses in time-slices of 9.6 ns. In the Radial chambers both ends of each wire-pair are instrumented, whereas in the Planar chambers the wires are instrumented at one end only.

When an event is triggered this history is scanned for regions containing significant raw data [2]. These regions together with a number of leading time-slices are then transferred to the next stage of the data acquisition, the QT analysis. This analysis performs a 'hit' search on these data, and for each hit found, corresponding to the ionisation left behind by a charged particle passing through the detector, a charge (Q) and time (t) are determined.

The QT analysis techniques for the Radial and Planar chambers are described separately below.

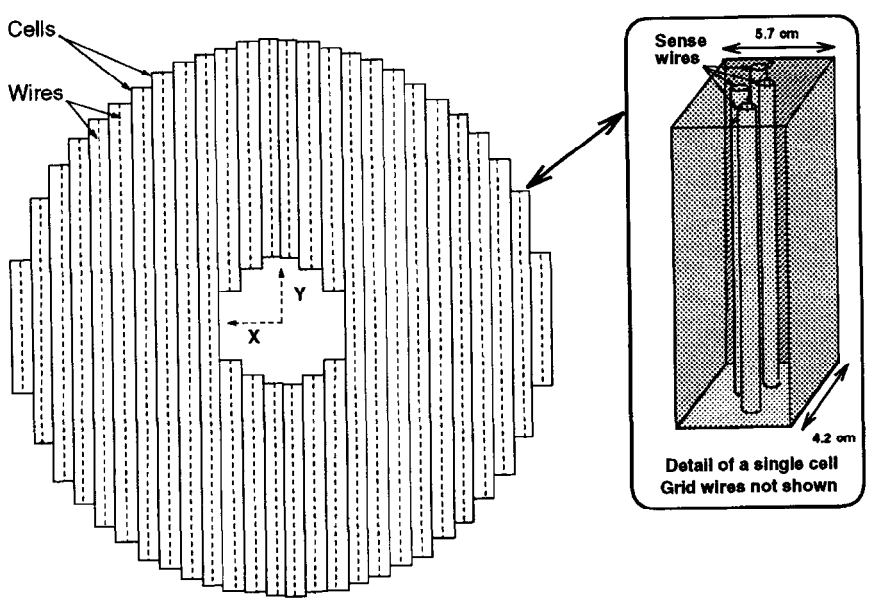

Fig. 5. Details of Planar cells.

3.1. Radial QT

The raw data are linearised, a pedestal level is determined and a search is then made for hits in each region containing significant data. Having found a hit, a time and charge are determined for each end of the wire-pair (+, −) separately. A single time for the hit is then calculated by taking a weighted mean of the two times:

$$t = (Q_+ t_+ + Q_- t_-)/(Q_+ + Q_-)\,. \tag{1}$$

Using a mean weighted by the charge reduces the influence of the degraded precision of the time calculated at the end of the wire-pair with the smaller pulse. Both charges are written out, allowing the later determination of the coordinate along the wire-pair by means of charge division. These steps are described in more detail below.

3.1.1. Hit search

The disposition of sense and field wires in the Radial chambers means that the charge arriving from a track through the cell, even for one at normal incidence, is spread over a period of time corresponding to 5 mm drift distance (the different geometry in the Planar cell results in the corresponding spread being over 1 mm). The Radial QT therefore uses a first electron method to avoid problems with anisochronicity, along with a strict requirement on the trailing edge of the pulse to avoid problems with resolved structure in an otherwise clean single hit.

A hit is defined as two or more time-slices above a threshold in the weighted difference of samples (weighted DOS), possibly with intervening time-slices below threshold, followed by at least two time-slices where the weighted difference of samples is negative, without intervening time-slices above threshold.

The difference of samples (DOS) is defined as [7]:

$$DOS_i(n) = \mathrm{FADC}_i(n) - \mathrm{FADC}_i(n-1)\,, \tag{2}$$

where $\mathrm{FADC}_i(n)$, the pulse height, is the linearised content of the nth time-slice from end i ($\pm$) of the wire-pair. The weighted DOS, $W(n)$, is then defined as the product:

$$W(n) = \left| \sum_{i=+-} (\mathrm{FADC}_i(n) - P_i - A) \right| \times \sum_{i=+-} \mathrm{DOS}_i(n)\,, \tag{3}$$

where the pedestal level, P_i, is calculated from the flat region of data at the beginning of the sample and A defines an arbitrary offset from this pedestal level which allows tuning of the detection efficiency for small hits. An initial estimate of the time of the hit at each end of the wire-pair is defined as the start of the time-slice of the first maximum in $\Sigma_{i=+-}\,\mathrm{DOS}_i(n)$ in the data above threshold in $W(n)$.

This method of locating hits has advantages compared to conventional techniques, such as the simple threshold cut employed by the scanner, or derivatives such as a threshold cut in DOS, which do not cope well with a non-uniform background:

- using the combined information from both ends of the wire-pair, namely the total charge of the hit, makes the hit search insensitive to the effects of charge division along the wire-pair length (this length is sufficiently small that propagation delays along the wire-pair may be neglected at this stage);
- using the pulse height and DOS simultaneously reduces the sensitivity to vagaries in the rise time of the pulse. Overall $W(n)$ forms a strong signal for all but the smallest pulses but is relatively insensitive to an oscillating or gently rising baseline;
- combining the information from both ends of the wire-pair reduces the sensitivity to electronic pickup, which tends to be out of phase at either end of the wire-pair;
- $W(n)$ is also sensitive to any further pulses that may be behind the initial detected pulse.

3.1.2. Time determination

For each hit found a time is calculated separately for each end of the wire-pair using a first electron timing method. The local DOS maximum within two time-slices of the initial estimate of the hit time defined above is found and used as the basis for the calculated time. This is formed by projecting the gradient given by the DOS of this time-slice back down to the pedestal level as shown in Fig. 6. In essence this is a form of constant fraction discriminator, with the fraction set at zero [8]. The distribution of the offset of this time relative to the start of the time-slice containing the local DOS maximum is shown in Fig. 7.

The assumption that the time-slice of maximum DOS is the nearest time-slice to the "true" time of the hit, along with there being no correlation between the 104 MHz clock and the true hit time, leads to the conclusion that the distribution in Fig. 7 should ideally be a "top hat" function of unit width, corresponding to the distribution within a single time-slice. With the assumption that this offset is a monotonic function of the true time, the calculated time may be improved by applying a trans-

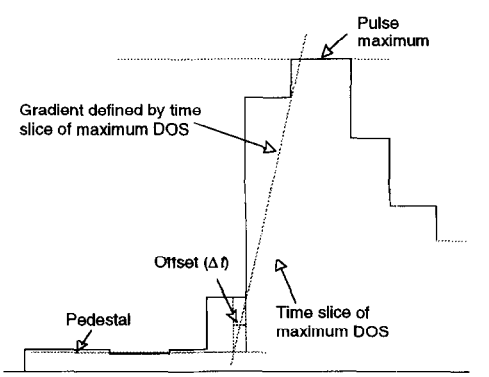

Fig. 6. Time determination using a first electron method.

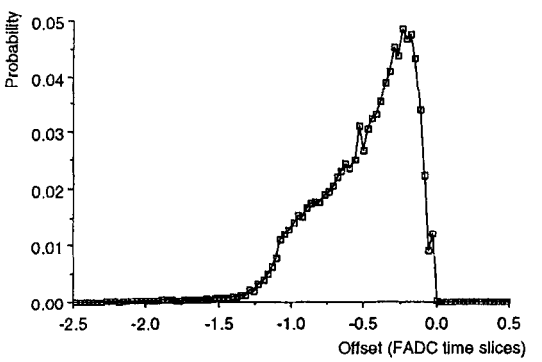

Fig. 7. Distribution of the leading edge intercept with the base line, relative to the start of the time-slice of maximum DOS.

formation to the observed offset such that the resultant distribution does have the desired "top hat" shape [9].

Illustrated in Fig. 8 are the cumulative probability distributions for the observed offset distribution and for the desired "top hat" distribution. The transformation from the first to the second is obtained by taking the cumulative probability value corresponding to a particular offset in the first distribution and using this probability to read off the corrected offset in the second distribution, as illustrated by the line in the figure.

The above analysis is valid for each end of the wire-pair separately. For the average time for the hit derived as in Eq. (1) the effect of the weighting by charge in the time determination is taken into account by using a charge-weighted intercept distribution and then proceeding as outlined above.

3.1.3. Charge determination and radius measurement

Reconstructing the radial coordinate of the hit by measuring the timing difference between each wire-pair end depends on the resistance–capacitance–inductance (RCL) distribution along the anode; in contrast charge

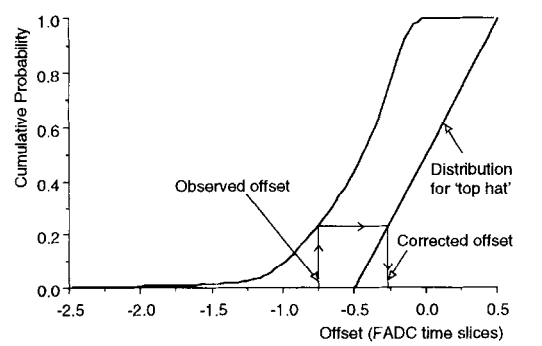

Fig. 8. Cumulative probability distribution corresponding to Fig. 7 for the first electron timing algorithm and for the desired "top hat" function. The observed offset is transformed to a corrected value as shown.

division depends only on the ratio of the resistances to either side of the impact point and is independent of the capacitance and inductance distribution [10]. For this reason the Radial chambers measure the radial coordinate by charge division, so that the wedge shape of the drift cell and the presence of the hub connection do not affect the intrinsic linearity of the measurement. This does however result in the radial coordinate measurement being sensitive to overlapping hits.

To obtain the charge at each end of the wire-pair the pulse height above pedestal is summed for 12 FADC time-slices, starting 2.0 time-slices before the hit time as calculated at that end of the wire-pair, using linear interpolation within a time-slice at each end of the range. Using a fixed interval relative to the time of the hit, rather than the data between two threshold values, results in the measured charge remaining closely proportional to the total charge. Were the integration interval allowed to vary, pulses which have a particularly long or high trailing edge would result in an overly large pulse integral and small pulses would be unnecessarily truncated, introducing extra systematic effects into the radial coordinate determination. The method of integration, the range and the offset of this range relative to the hit time have been tuned on data taken in a test beam [9].

3.1.4. Multiple hit analysis

Essentially the same techniques as described above are used in the case where multiple hits are resolved. The hits are analysed chronologically. The time for the first hit is calculated as above, and then the charges. The charge integration interval is however restricted if necessary to finish before the following hit. The response of the first hit is then removed from the data by taking the pulse height just before the start of the next hit and using this to subtract the tail of the earlier pulse, assuming an exponential decay. Slightly different decay constants are used depending on the observed coordinate along the wire-pair, to take into account the effect of the different RCL loads seen to each end of the wire-pair. Once this subtraction has been performed the analysis of the next hit is exactly the same as for the first, repeating this prescription until all hits have been analysed.

With the definition of a hit as given in Section 3.1.1 it is impossible to resolve hits separated by less than 4 time-slices, corresponding to about 1.2 mm; those separated by more than 6 time-slices are resolved with near 100% efficiency (Table 1). A conservative estimate of the two-track resolution is therefore close to 2 mm.

Table 1
Distribution of hit separations

Separation in time-slices	4	5	6	7
Number of hits	7112	49 543	105 016	102 151

Table 2
Hits and inefficiencies for the 12 wire planes of Radial Supermodule 0 for a typical run

z plane	Regions	Hits	No hit found [%]
0	29 526	29 201	12.9
1	46 224	60 137	3.6
2	47 160	66 244	2.1
3	48 134	68 797	2.1
4	48 236	69 546	1.9
5	48 423	70 011	2.0
6	49 041	71 181	2.0
7	48 880	71 154	2.1
8	46 955	67 633	2.0
9	47 291	67 812	2.2
10	46 958	67 879	2.0
11	46 374	70 867	2.8

3.1.5. Hit finding efficiency

An upper limit for the inefficiency of the QT algorithm can be determined from the fraction of raw data regions in which no hit is found. Note that the number of regions is wire dependent due to nonuniformity of the electric field, especially towards the front of the chamber. The total number of hits detected by the QT analysis in the regions of raw data is shown in Table 2. Also shown is the percentage of regions where no hit is found.

With the exception of the front wire, the proportion of regions of raw data passed to the QT analysis where no hit is subsequently detected is 2.2%. This rises to 12.9% for the front wire. Visual scanning of these regions of data cross-checking with the signal on adjacent wires, shows that a sizeable proportion of the empty regions genuinely should produce no hits. The hit finding efficiency is therefore better than 97.8% for wires 1–11.

3.2. Planar QT

The requirements on charge measurement in the Planars are less strict than in the Radials because no charge division is performed. A different scheme is therefore adopted in which the calculation of time and charge follow a strategy which is designed to be fast and robust in the presence of multiple hits.

3.2.1. Cluster search and charge determination

The cluster finding procedure is illustrated schematically in Fig. 9 which shows a cluster, as might be formed by two overlapping hits with a separation (1.3 mm) close to the limit of resolving power of the system.

After linearisation of the raw data a search is made for regions where the FADC bin contents exceed a threshold (a) defined by the pedestal (the mean of the first five scanned time-slices (b)) plus a fixed offset. Provided that at least four such adjacent time-slices are identified, the region is defined as a cluster (c), the bins above threshold are summed to form an estimate of the overall charge (Q), and pointers to the start and end of the cluster are passed to the following hit search step.

3.2.2. Hit search and time determination

A hit search is performed on each of the identified clusters. The procedure is illustrated in Fig. 10, which shows the same data as Fig. 9.

The characteristically fast rise time of the pulses (typi-

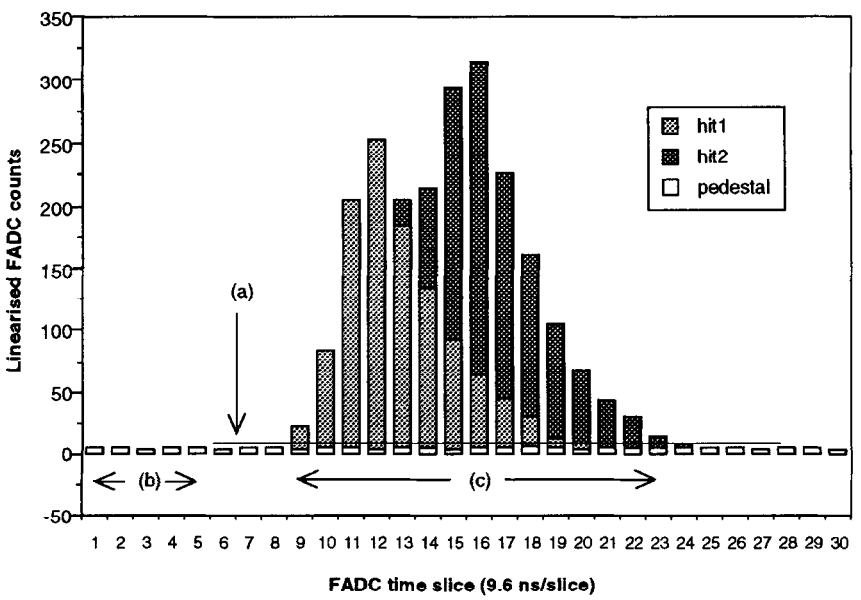

Fig. 9. Schematic identification of a cluster in the Planar FADCs. See text for definition of (a), (b) and (c).

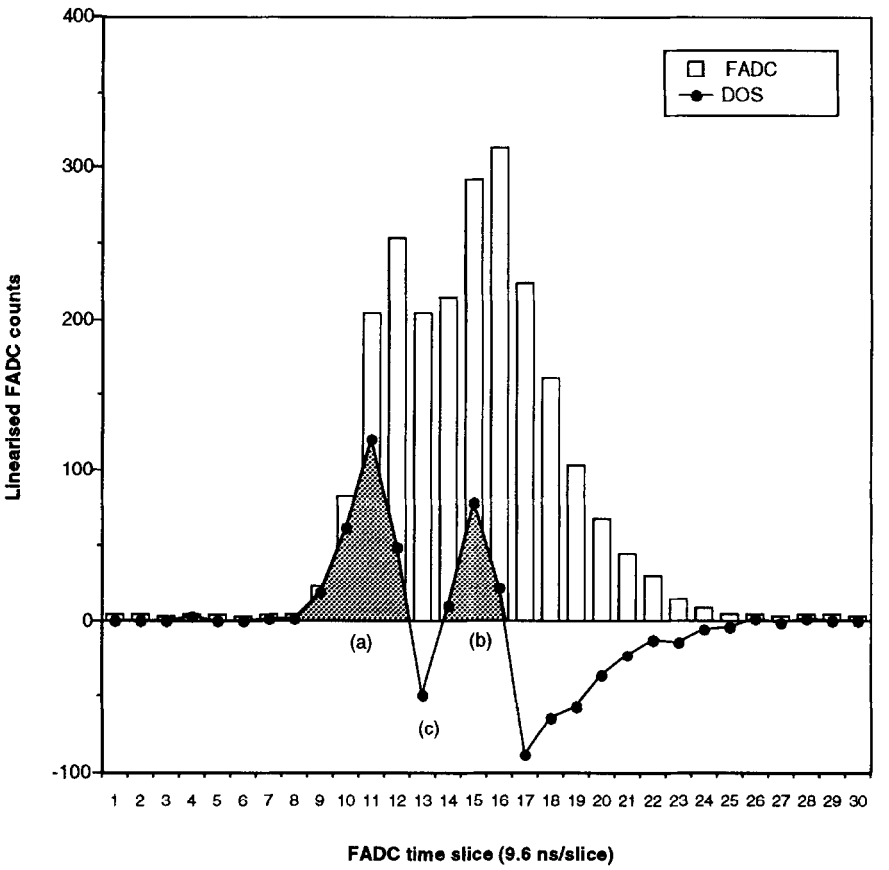

Fig. 10. Hit identification and timing using the DOS method applied to a cluster. See text for definition of (a), (b) and (c).

cally 30 to 40 ns) associated with charged particle ionisation can be used as a trigger for hit identification. This is achieved, as for the Radial chamber analysis, by formation of a DOS by numerical differentiation of the FADC spectrum (Eq. (2), applied to single-ended readout). The rising edges of pulses reveal themselves as sharp positive peaks in the resulting DOS spectrum ((a) and (b) in the figure). Hits are defined as groups of at least two adjacent bins satisfying two conditions:

- each bin in the group must have DOS greater than zero;
- the hit amplitude, $A = \Sigma_{\text{group}} \text{DOS}(n)$, must exceed a fixed threshold.

A single negative DOS bin ((c) in the figure) is sufficient to resolve hits with this algorithm.

The time of each hit, relative to the start of the scanned range in units of FADC bins, is computed as the weighted average over the bins in the group:

$$t = \frac{\sum n \cdot \text{DOS}(n)}{A}. \tag{4}$$

This technique is particularly stable in the presence of background, which is removed up to first order by the explicit differentiation in the DOS. Provided that the background, b, for example the trailing edge of an earlier hit, can be approximated as linear ($b \approx a + c \cdot n$) across the leading edge of the pulse, it contributes a constant level c to the DOS with no significant shift in the hit timing. The two-track resolution is similar to that for the Radial chambers.

3.2.3. Charge estimation for multiple hits

The charge of each identified cluster is distributed between the hits (k) found in the cluster in proportion to their amplitudes:

$$Q_k = QA_k \left\{ \sum_k A_k \right\}^{-1}. \tag{5}$$

The quantities used in this calculation are already available to the QT analysis from the cluster and hit finding stages, so that determination of Q_k by this method minimises the amount of additional computation. This minimisation can be important when the required rate of raw data reduction is high, but costs some degradation in Q_k estimation because of the implicit assumption that the pulse shape is constant (so that Q_k is proportional to A_k). This is tolerable

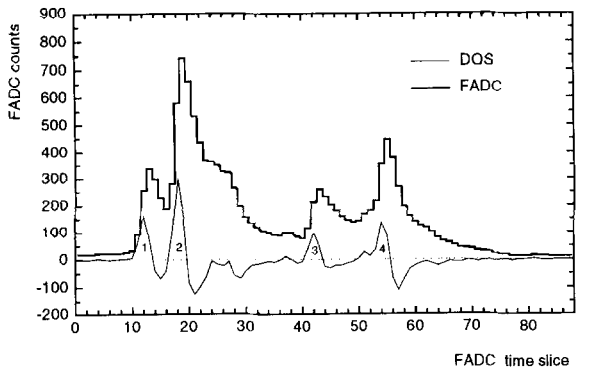

Fig. 11. Hits identified by the Planar hit finding algorithm in FADC output obtained under normal H1 operating conditions. Hits 1 and 2 are separated by 1.9 mm.

for the Planar chambers, which do not determine position by charge division.

3.2.4. Hit finding efficiency

The thresholds used in the Planar QT algorithm have been tuned on e–p interaction data to optimise the hit finding efficiency and noise rejection under normal H1 operating conditions. The method, which involves statistical determination of the number of hits which form aligned combinations from charged particles traversing single Planar cells, is described in Section 4.5. This hit finding efficiency is monitored continuously and is normally greater than 95%. Its high value is confirmed by scanning of Planar FADC spectra from the same data sample, an example of which is shown in Fig. 11, where excellent agreement is found between the QT identified hits and the leading edges which are evident by eye.

4. Calibration and monitoring of the drift chambers

The drift times from the QT analysis must first be corrected for timing offsets and then converted into drift distances. When combined with the known location of the sense wires in the H1 coordinate frame, these provide preliminary data for use by the pattern recognition and track fitting software. Corrections for track inclination to the wire plane and time-of-flight are made once approximate track parameters have been determined. Section 4.1 describes aspects of the time-to-distance relation which are common to both the Radial and Planar drift chambers. Special features of the two different types of drift chamber, together with the methods used to calibrate and monitor them, are described in Sections 4.2 to 4.5. Section 4.6 shows how the calibration and monitoring techniques are applied in practice.

4.1. Time-to-distance model

The following model of the drift cells is used to motivate the choice of time-to-distance function. The configuration of the drift chambers is depicted schematically in Fig. 12. The electric field lines lie in planes perpendicular to the sense wire as shown in Fig. 12b. For drift distances, s, greater than about 0.5 cm (measured perpendicularly to the sense wire in the same z plane) the electric field is constant in magnitude and orthogonal to both the sense wire and the z direction. Closer to the wire, the electric field increases like $1/s$ and turns to point radially into the wire. To a good approximation, the isochrones are semicircular. It is assumed that the ionisation clusters produced nearest to the point where the track is tangent to the isochrones arrive first and define the leading edge of the pulse. If the track crosses the drift cell perpendicularly this point is at the same z as the wire. For track reconstruction purposes, the drift coordinate of a point on a track is defined as the perpendicular distance from the track to the wire at the z of the wire. The drift distance is first estimated from the measured drift time assuming that the track crosses orthogonally. For inclined tracks, a correction to the estimated drift distance must therefore be applied:

$$\delta s = d(\sec \Psi - 1) \tag{6}$$

where d, the radius of the isochrones, is approximately equal to s_1, the distance from the wire at which the ionisation begins to drift radially and Ψ is the angle the track makes with the plane containing the sense wire and the z direction (see Fig. 12b). Close to the wire, d is replaced by the distance of closest approach of the track to the wire. The correction is made in the final track fit once the track inclination angle is known.

For ionisation drifting towards the sense wire in the same z plane as the wire the absolute value of the drift velocity remains approximately constant along the drift path. The magnetic field is everywhere orthogonal to the sense wires and to the electric field. The ionisation drifts towards the sense wire at a fixed Lorentz angle, α, and

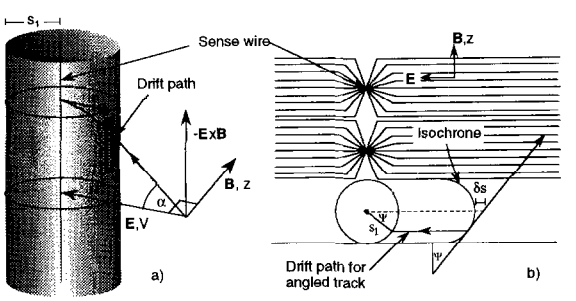

Fig. 12. The drift path for ionisation produced at the centre of a cell (a) and from an inclined track (b).

then, close to the wire, the angle decreases as the electric field increases, as shown in Fig. 12a. The component of the drift velocity perpendicular to the wire therefore increases as the wire is approached. To an adequate approximation, since E is inversely proportional to the drift distance, s, for $s < s_1$ and B is constant [11],

$$\tan\alpha \sim |B|/|E| \equiv \beta s \,. \tag{7}$$

Then, the perpendicular component of the drift velocity is given by

$$V(s) = V_0 \cos\alpha(s) = \begin{cases} \dfrac{V_0}{\sqrt{1+\beta^2 s^2}} & s \le s_1 \\ V_1 \equiv \text{constant} & s > s_1 \end{cases} \tag{8}$$

where V_0, the perpendicular component of the velocity at the wire, is equal to the magnitude of the drift velocity (assumed constant throughout the drift space in this model).

The constant β can be evaluated in terms of V_0 and V_1:

$$\beta = \frac{\sqrt{V_0^2 - V_1^2}}{V_1 s_1} \,. \tag{9}$$

The time required to drift from a distance s to the wire is given by:

$$t(s) = \int_0^s \frac{\mathrm{d}s}{V(s)}$$

$$= \begin{cases} \dfrac{1}{2\beta V_0}\{\beta s\sqrt{1+\beta^2 s^2} + \ln(\beta s + \sqrt{1+\beta^2 s^2})\} & s \le s_1 \\ t(s_1) + \dfrac{s - s_1}{V_1} & s > s_1 \end{cases} \,. \tag{10}$$

This equation cannot be inverted in closed form, but an approximation in which the perpendicular component of drift velocity (hereafter called drift velocity) increases linearly from V_1 to V_0 as s decreases from s_1 to zero yields drift distances which differ from it by at most 10 μm. Fig. 13 shows the drift velocity as a function of s together with the linear approximation. Deviations from this model and the methods used to determine the parameters are discussed in Sections 4.2 and 4.3. Note that, with mean drift distances of order 2 cm, the mean drift velocity, $\langle V \rangle$, must be calibrated to better than 0.5% in order to keep systematic errors on the reconstructed distances to less than 100 μm.

4.2. Calibration of the Planar chambers

The geometry and staggered wires of the Planar drift cells (see Section 2.2) allow for a straightforward approach to monitoring and calibration which utilises the known dimensions and symmetries of the cells to maximum effect. In particular it is possible to form statistical checksums which give a direct measure of chamber performance and data quality without the need for track reconstruction. These techniques permit effective monitoring and calibration of the chambers as the data accumulate.

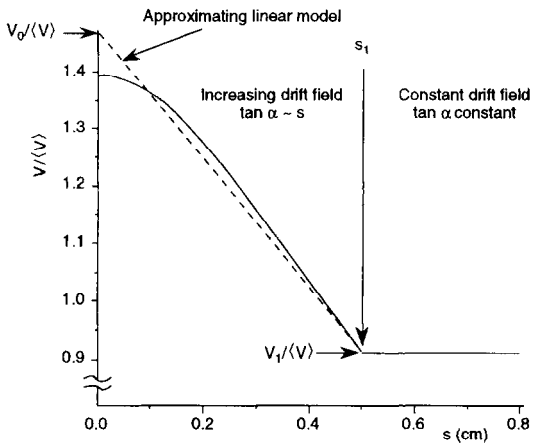

Fig. 13. Drift velocity as a function of drift distance. The curve corresponds to the model given by Eq. (8).

4.2.1. Time-to-distance function for the Planar chambers

The Planar QT algorithm (see Section 3.2) processes the FADC information from four adjacent wires (one Planar cell) in a single call, returning the time (t) and integrated pulse size (Q) for every hit found. These times are then transformed to drift distances, $s(t)$ (Section 4.1).

The electric field in the Planar cells is accurately uniform, at ~1 kV/cm, over 80% of the 28.1 mm drift range, but rises rapidly in the last 5 mm of drift, closest to the sense wire. This causes nonlinearity in $s(t)$, through the mechanism described in Section 4.1 and Fig. 13. The effect of this nonlinearity is clearly visible between t_0 and t_1 in the Planar drift time distribution shown in Fig. 14. The

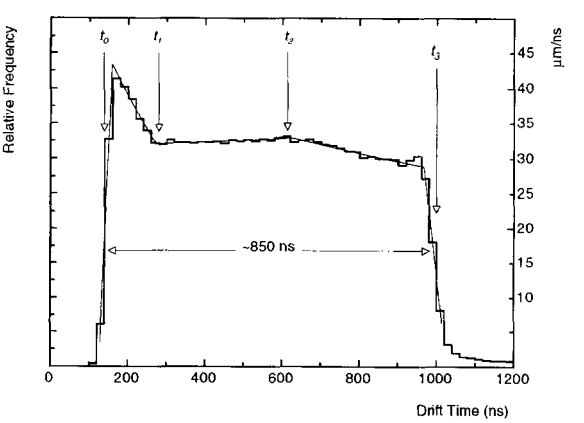

Fig. 14. Typical Planar drift time distribution with the four knots t_k indicated. The approximate velocities on the right hand scale are discussed in the text.

origin of the knot at t_2 is not understood. The small rise before t_3 is due to double counting of hits from tracks crossing the cathode plane.

In practice the time-to-distance relation is parametrised in terms of a local velocity which varies linearly with drift distance, s, over regions $s_k < s < s_{k+1}$, where k labels the knots, in a way which corresponds to the structure which is visible in the drift time distribution (Fig. 14):

$$V(s) = V_k + \frac{(s - s_k)}{\tau_{k+1}}, \qquad \tau_{k+1} = \frac{(s_{k+1} - s_k)}{(V_{k+1} - V_k)}. \tag{11}$$

Defining

$$\Delta t_k^{k+1} = \text{drift time from } s_{k+1} \text{ to } s_k = \int_{s_k}^{s_{k+1}} \frac{ds}{V(s)} = \tau_{k+1} \cdot \ln\left(\frac{V_{k+1}}{V_k}\right) \tag{12}$$

the integrated drift time, t', from a point $s_k < s < s_{k+1}$ to the sense wire is

$$t'(s) = (t_k - t_0) + \tau_{k+1} \cdot \ln\left\{1 + \frac{(s - s_k)}{\tau_{k+1} \cdot V_k}\right\} \tag{13}$$

$$\text{with } (t_k - t_0) = \sum_{n=1}^{k} \Delta t''_{n-1}$$

which can be inverted to obtain a parametrised analytic form for the time-to-distance relation, valid for times in the region $t_k < t < t_{k+1}$:

$$s(t) = s_k + V_k \tau_{k+1} \cdot \left\{\exp\left[\frac{(t - t_k)}{\tau_{k+1}}\right] - 1\right\}, \tag{14}$$

where $t = t' + t_0$ is the measured drift time.

Two sets of four velocities ($V_k^{\text{in(out)}}$, $k = 0, 1, 2, 3$ for the inner (outer) pair of wires in a cell) and two asymmetry parameters are sufficient, with the above linear local velocity model, to provide a good description of the drift properties of a Planar cell. Typical values are shown in Table 3. The asymmetries, which are caused by electrostatic differences associated with the staggered wires, are used to scale the local velocities by $(1 \pm a_k)$ depending on whether the wire is staggered away from $(-)$ or towards $(+)$ the hit [12]. The a_k are determined using the C_2 check-sum described in the next Section.

These local drift velocities have been determined, in the first instance, by a direct fit to the drift time distribution on the inner and outer wires, with the assumption that the source distribution of hits is uniform in drift distance, s;

$$\frac{dN}{ds} = \rho = \text{constant} \tag{15}$$

so that

$$\frac{dN}{dt} = \frac{dN}{ds} \cdot \frac{ds}{dt} = \rho V(s). \tag{16}$$

The approximate local velocities which follow from this assumption, in μm/ns, can be read from the right hand scale of Fig. 14. The fit uses Eq. (16), with Eqs. (11) and (13) in a χ^2 minimisation having t_0, $V_k^{\text{in/out}}$ and $s_k^{\text{in/out}}$ as free parameters but with $s_0^{\text{in/out}}$ fixed at zero and $s_3^{\text{in/out}}$ fixed at the cell width (28.1 mm). When s_1^{in} and s_1^{out} were fitted independently they were found to be the same; subsequently they have been constrained to be equal. In addition there are four free parameters which are required to account for resolution effects at the front and back edges of the inner and outer drift time distributions. This gives a total of 16 free parameters to fit about 100 data points (two plots like Fig. 14 where the smooth curve shows the result of such a fit). The values obtained from such fits (including the knot at s_2) have been confirmed by using the resulting $s(t)$ parametrisation in the track reconstruction to check that variations in the V_k show the track segment fit residuals to be at a minimum and the number of found Planar track segments to be at a maximum.

Table 3
Calibrated Planar time-to-distance parameters

k	a_k	s_k^{in} [μm]	V_k^{in} [μm/ns]	s_k^{out} [μm]	V_k^{out} [μm/ns]
0	0.028	0	44.85	0	46.47
1	0.004	5025	32.87	5025	31.74
2	0.0	16 360	33.06	17 080	32.93
3	0.0	28 100	28.87	28 100	29.12

4.2.2. Calibration and monitoring

Fits of the above type are not performed for every run. Instead, having determined the $V_k(N)$ and mean velocity $\bar{V}(N)$ for run number N, the local velocities for later runs are determined by scaling;

$$V_k(N + m) = V_k(N) \times \frac{\bar{V}(N + m)}{\bar{V}(N)}. \tag{17}$$

The mean velocities, $\bar{V}$, are determined to better than ±0.3% every two hours on average during normal e–p running from the width of the drift time distribution and the known cell size (cell width/drift time width ≈28.1 mm/850 ns ≈ 33 μm/ns).

Typical results from run-by-run calibration are shown in Fig. 15. The 88 calibrated runs shown there span four days, have a mean drift velocity of 32.854 μm/ns and an rms scatter of 0.06 μm/ns. The smallness of this 0.2% rms fluctuation confirms the intrinsic statistical accuracy of the calibration method and the excellent stability of the Planar chamber operating conditions and gas mixture control system [2].

A complementary method for monitoring the stability of drift velocity, which also provides information on intrinsic resolution and data quality, has been developed by making use of the ±300 μm stagger of the Planar sense wires.

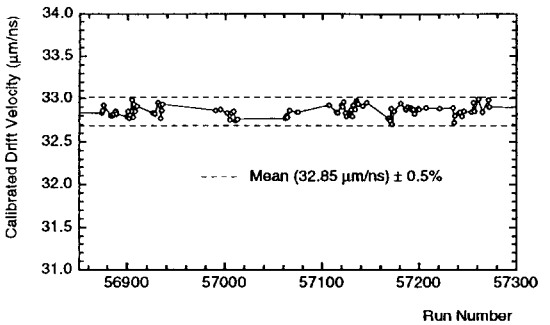

Fig. 15. Calibrated mean drift velocities for the Planar chambers.

With some obvious but approximate assumptions concerning linearity and symmetry a charged track of momentum ≥ 20 MeV/c will produce the following drift times:

$$
\begin{aligned}
T_1 &= \frac{1}{V}|d_1| \\
T_2 &= \frac{1}{V}|d_1 + \delta \sin(\Psi) + 2\gamma\Lambda| \\
T_3 &= \frac{1}{V}|d_1 + 2\delta \sin(\Psi)| \\
T_4 &= \frac{1}{V}|d_1 + 3\delta \sin(\Psi) + 2\gamma\Lambda| .
\end{aligned}
\tag{18}
$$

Here d_1 is the perpendicular (drift) distance from the track to wire 1, δ is the wire spacing (6 mm), Ψ is the angle of the track relative to the plane defined by the wires (Fig. 12), Λ is the stagger of the wires (± 300 μm in the s direction), $\gamma = \pm 1$ depending upon the relative sign of Λ and s for that wire and V is the component of drift velocity in the s direction. Provided that s has the same sign for all four wires, i.e. that the track does not cross between the wires, the following check-sums are valid;

$$
\begin{aligned}
C_1 &= (T_2 - T_1) - (T_4 - T_3) = 0 \\
C_2 &= \tfrac{3}{4}(T_3 - T_2) - \tfrac{1}{4}(T_4 - T_1) = \frac{2\Lambda \cdot \gamma}{V} .
\end{aligned}
\tag{19}
$$

For tracks emerging from the e–p interaction point (on the z axis), the probability of crossing between the wires is very small (of order 300 μm/3 cm ≈ 1%), so the distribution of C_1 shown in Fig. 16a shows a sharp peak close to zero. Fig. 16b shows the distribution of C_2 for $|C_1| <$ 24 ns, with the peaks corresponding to $\gamma = \pm 1$ clearly visible, demonstrating an ability of the Planar chambers to resolve the left-right drift ambiguity. The plots of C_1 and C_2 are for cells with one and only one hit/wire.

An estimate of the drift velocity can be obtained from the fitted separation of the peaks in the C_2 distribution. The ratio of the calibrated velocity, determined from the width of the drift time distribution, to that extracted by this method, is shown in Fig. 17.

It is clear that the velocity determined from the peak

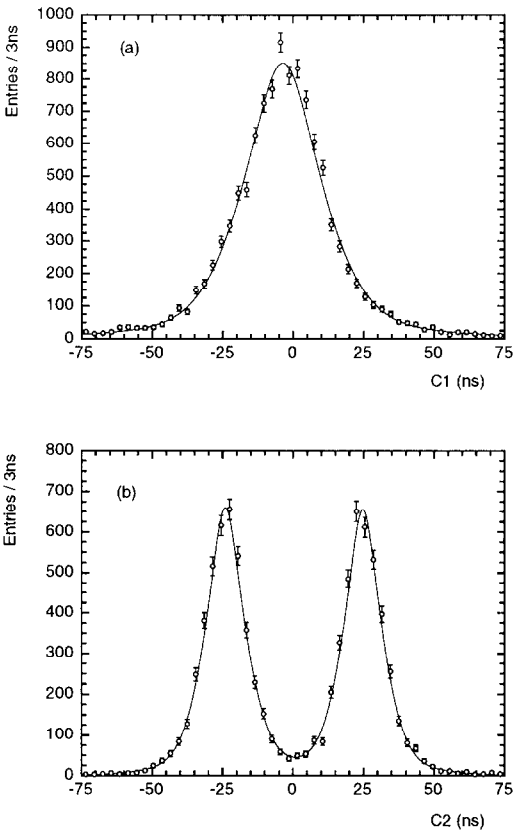

Fig. 16. (a) Check-sum C_1 (b) Check-sum C_2. The fitted curves are generalised Breit–Wigner distributions with a smooth background [19].

separation in the plot of check-sum C_2 is significantly lower than the true velocity. This is known to be due to a small, stagger related, electrostatic asymmetry in the drift cell [12], which is taken into account when formulating the time-to-distance relation through the asymmetry parame-

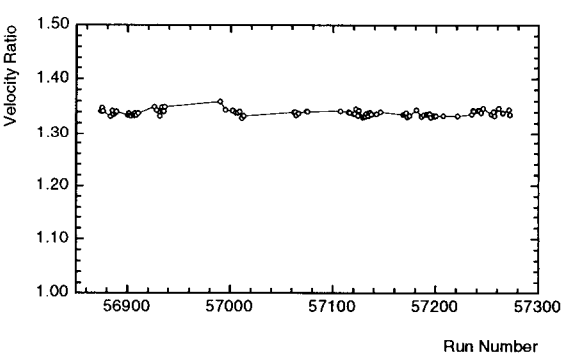

Fig. 17. The ratio of the drift velocity from the width of the drift time distribution to that determined from the C_2 check-sum versus run number.

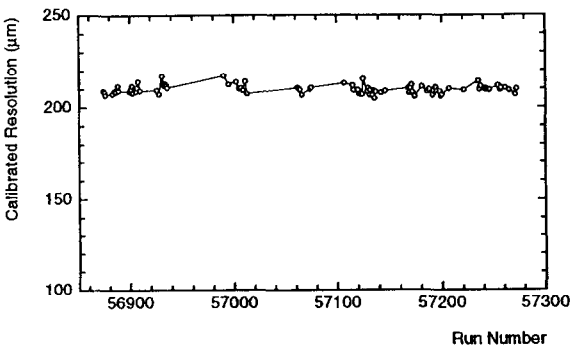

Fig. 18. Mean resolution of Planar chambers from the C_2 checksum.

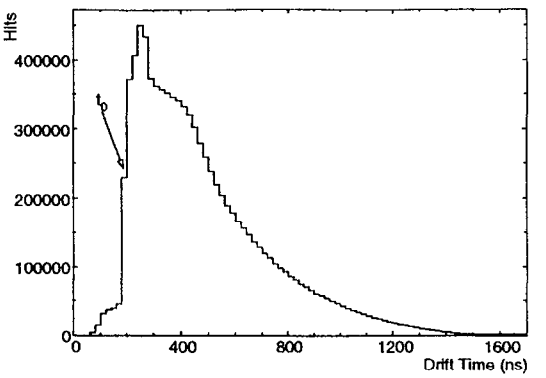

Fig. 20. Typical drift time distribution in the Radial chambers.

ters, a_k, of Table 3. The constancy of the ratio verifies that the above asymmetry does not change with time and gives independent confirmation of the drift velocity stability.

4.2.3. Planar drift measurement precision

From the fitted widths of the peaks in Fig. 16 an estimate of the single hit resolution can be made; typical results are shown in Fig. 18. The functional dependence of resolution on drift distance can be established by analysing the C_2 distribution from hits in different bands of drift distance. These results are shown in Fig. 19 with the best fitting parametrisation (s in cm, σ in μm)

$$\sigma^2 = 165^2 + s92.3^2 + 807^2\, e^{-10.5s} \qquad (20)$$

superimposed. The second term models the effect of diffusion with the third term parametrising the effect of nonuniform drift properties close to the sense wires.

4.3. Calibration of the Radial drift chambers

The wedge-shaped geometry of the Radial drift cell means that the drift time distribution cannot be directly used to obtain a measure of the average drift velocity as is the case in the Planar chambers. A typical drift time distribution is shown in Fig. 20. The leading edge of the distribution is well-defined and can be used to determine t_0. The overall shape however is complex and cannot be simply mapped into drift velocities. It arises from the wedge shape of the drift cells and nonuniform radial distribution of the hits. In addition, every sense wire penetrates the region of high hit density at small radius so that the probability of hit loss from two-track overlap is high and depends on the drift distance. (Hits at small drift distances are more likely to be lost, whatever their radii, than hits at large radii and large drift distance.) The density and distribution of hits in radius varies with beam and trigger conditions so that a fixed shape is not expected for the drift time distribution, even if the drift velocities remain constant.

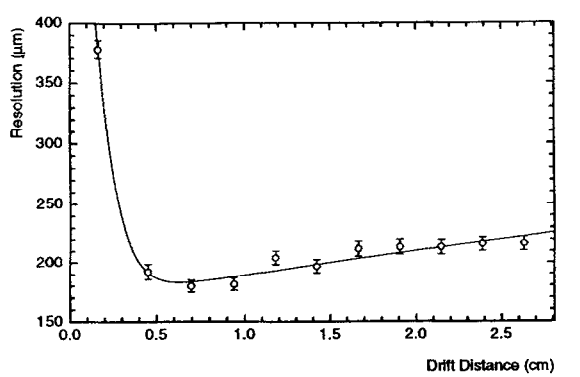

Fig. 19. Single hit resolution as a function of drift distance in the Planar chambers. The smooth curve is given by Eq. (20).

4.3.1. Time-to-distance function for the Radial chambers

The time to distance function in the Radial chambers is determined by using tracks reconstructed using the Planar chambers after calibration to predict the true drift distances of hits in the Radials. These distances can then be compared directly with the measured drift times (after correction for an overall timing offset and propagation time along the sense wires and signal cables). Fig. 21 shows the drift time, scaled by a nominal drift velocity, as a function of predicted drift distance obtained by this method.

The perpendicular component of the drift velocity is, to a good approximation, independent of both drift distance and radius in the region ≥0.5 cm from the sense wires; it increases close to the wire as expected from the model discussed in Section 4.1 which assumes that the magnitude of the drift velocity remains constant. This approximation may fail within 2 mm from the wire where the electrostatic field is large and the magnitude of the velocity may change significantly. The same parametrisation as that used for the planar chambers (Eq. (14)) is adopted, but only three knots

Table 4
Typical calibrated time-to-distance parameters for the Radial drift chambers showing (a) overall parameters and (b) wire-plane dependent velocity correction factors

k	a_k	s_k [μm]	V_k [μm/ns]
(a)			
0	0.0345	0	61.63
1	0.0	4950	37.51
2	0.0	∞	37.51

(b)												
Wire	0	1	2	3	4	5	6	7	8	9	10	11
Factor	0.989	0.999	1.002	1.004	1.004	1.004	1.004	1.004	1.004	1.004	1.004	0.985

and three velocity parameters are needed (Table 4(a)). Note that the last knot at s_2 is purely formal: the velocity is assumed to be constant for drift distances greater than s_1. The appropriate limiting forms of Eqs. (11)–(14) for $\tau_k \to \infty$ are used to compute the drift distance in this region.

Data like those in Fig. 21 are obtained for each run containing a reasonable number of events (~10 000) and are used to determine the velocity V_1. Independent straight line fits are made for positive and negative drifts in the range $0.6 \leq |s| \leq 3.5$ cm. The velocity is calculated from the weighted mean of the two slopes. A precision of about 0.2% is obtained. The velocity V_0 and location of the knot point s_1 can also be deduced from the same data. To a good approximation, these are found to scale with V_1 and a separate run-by-run determination is not necessary.

The electrostatic field configuration is not identical for all the wires in the Radial chambers. Consequently the average drift velocities near the front of the drift chamber are significantly lower than in the middle. These inhomogeneities are treated by applying scaling factors to the velocities on each of the twelve wire planes (Table 4(b)). As is the case for the Planar chambers, an asymmetry arising from the wire stagger is seen and is corrected for by applying a different scale factor to the velocities for hits on wires staggered towards or away from the track. This correction can only be applied once the sign of the drift coordinate has been resolved by the reconstruction software. These characteristics, including the wire-dependence of the drift velocities, have been qualitatively confirmed by an electrostatic simulation of the drift chambers using the GARFIELD [13] program.

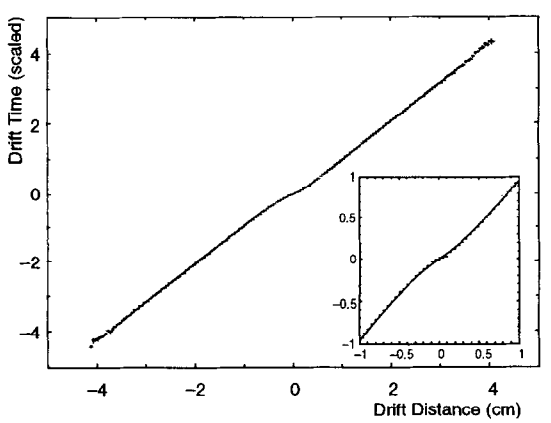

Fig. 21. Scaled drift time versus predicted drift distance. The insert shows the region at short drift distances.

4.3.2. Monitoring of the drift velocities in the Radial chambers

The above technique can be used as a monitor of the drift velocities only after track reconstruction has taken place. A fast monitor of changes in parameters is desirable in order to avoid mis-reconstruction of the tracks and the need to reprocess the data. To this end, some of the techniques already described for the Planar chambers are exploited.

Although no drift velocity information can be extracted from the drift time distribution alone, by making use of the charge division measurement it is possible to make drift time distributions in slices of radius, for which the drift cells have approximately constant width and so are more akin to those in the Planars. This allows the determination of the maximum drift time as a function of radius. Since the cell is wedge-shaped this time should increase linearly with radius given that the drift velocity is constant in the relevant region away from the sense wire. The slope is thus a direct measure of the drift velocity in the constant drift field region. A fit is performed over a restricted range, $30\text{ cm} < R < 60\text{ cm}$, in order to avoid end-effect distortions. Fig. 22 shows the location of the maximum drift time as a function of the radius, for two different gas mixtures, with the linear fits superimposed. The method is vulnerable to the imprecision of the radius measurement which smears the back edge of the drift time distributions. In addition, the imprecision itself depends on the hit density and so beam and trigger conditions can affect the result. Also, as a result of the Lorentz angle, the linear relationship depends on which side of the wire plane the hit originated and this cannot be determined at the single hit level. Consequently this method gives a drift velocity with an uncertainty of about 1%.

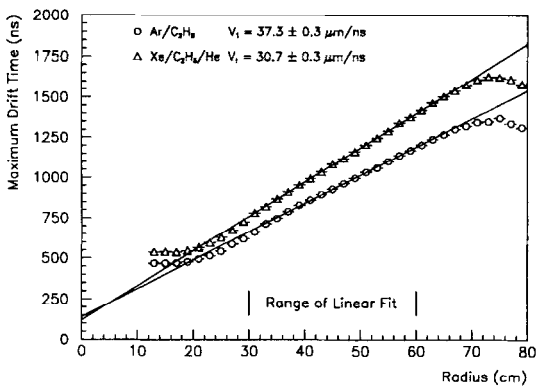

Fig. 22. Maximum drift time versus radius for two gas mixtures.

A Radial cell has 12 wires in depth; these can be taken in groups of four and the same check-sums as for the Planars can be calculated and monitored. The C_2 check-sum gives another measure of the drift velocity. The relationship between this velocity and the average drift velocity in the cell differs from that in the Planars because of the differing disposition of field wires. The run to run variation in this drift velocity is about 0.5% during stable periods of running and the method is less susceptible than the drift time versus radius method to beam conditions.

Fig. 23 shows the drift velocity measurements obtained for a series of data runs by the above methods. The ratios of the different velocity parameters remain constant from run to run so that the fast monitoring methods can be used to effect a rapid recalibration in the event of a significant change in operating conditions (see Section 4.6).

4.3.3. Calibration of the charge division measurement

Planar-based tracks are also used to calibrate the determination of the radial coordinates of the hits by charge division. The charge division measurement is not sensitive to the absolute charges, so frequent run-dependent calibrations are not needed for this purpose. The relative gains of the preamplifiers at the two ends of the wire-pair are measured using test-pulses, and resistances and resistivities were measured as part of a full chamber survey before installation. The measured relationship between the charge division variable $(Q^+ - Q^-)/(Q^+ + Q^-)$ and radius is linear.

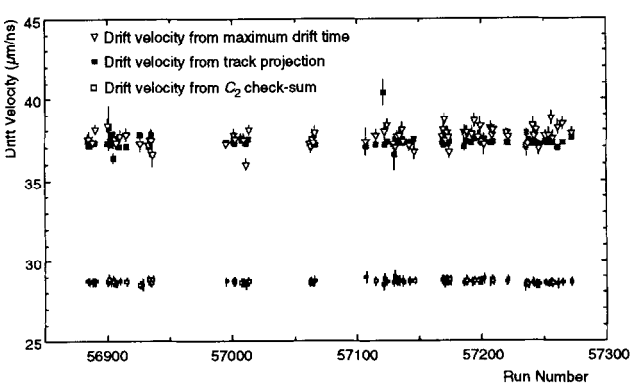

Fig. 23. Drift velocity measurements for a series of runs from the three methods.

4.3.4. Precision of the drift and radius measurements

Estimates of the single hit drift resolution and its dependence on drift distance are obtained from an analysis of C_2 check-sum distributions as described for the Planar chambers in the previous Section. Using the same functional form to parametrise the resolution gives (Fig. 24)

$$\sigma^2 = 1.9^2 + s127.7^2 + 377^2 e^{-2.21s}, \quad (21)$$

giving a mean resolution ≈ 180 μm.

The method of track projection from the Planar chambers is used to check the radial coordinate determination. The best resolution of about 1.5 cm is achieved only for the larger pulses. The average resolution for isolated hits is 3–4 cm. More seriously, because of the high hit density, a substantial fraction of hits overlap. The radius measurement may be significantly degraded for such hits.

4.4. Determination of t_0

Before application of the time-to-distance functions, various corrections are applied to the times determined by the QT analysis. An average offset from the trigger time, t_0, is determined for each data run by locating the leading edge of the drift time distribution of the hits. This is done by numerical differentiation of the drift time distribution to obtain a positive peak corresponding to the rising front edge. The fitted time of this peak is used to define the timing offset to an accuracy of ~0.5 ns for a typical run.

Fig. 25 shows the t_0 values, as determined by this method, over a two month period in 1993. Discontinuous changes, due to known hardware modifications, are clearly

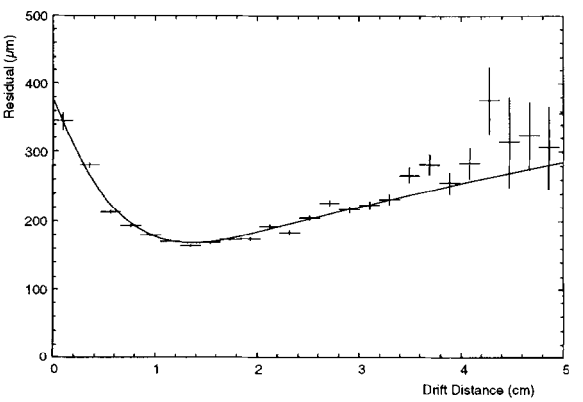

Fig. 24. Single hit resolution as a function of drift distance in the Radial chambers.

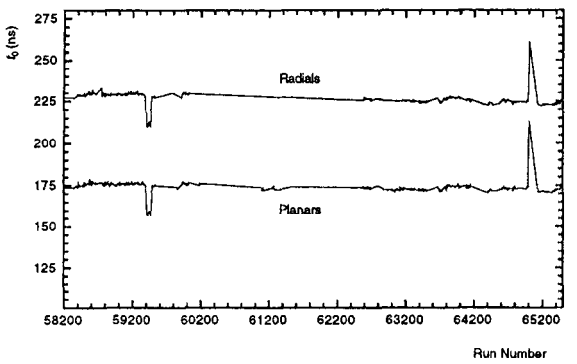

Fig. 25. t_0 values from the analysis of Radial and Planar drift times versus run number. The solid lines join the measurements. The Radial t_0 has been increased by 40 ns for clarity.

visible. Fluctuations at the nanosecond level, due to variations in the mean position of the e–p interaction point, are closely followed by this method.

Relative timing offsets between the sense wires are evaluated using test-pulses and only require occasional updating when the hardware is changed. Corrections for the time of flight from the event vertex to the hit position are made in the final fit. Timing corrections are also made for propagation time along the sense wire. In the case of the Radial drift chambers, the correction takes into account the weighting procedure described in Eq. (1) and uses the radius determined by charge division. For the Planar chambers the correction is made during the final fit (Section 7).

4.5. Monitoring of the hit finding efficiency

A measure of the hit finding efficiency can be obtained by using a modified form of the C_2 check-sum analysis (Section 4.2.1). Groups of four adjacent wires are selected which have exactly one hit found on each of the first and last sense wires. If a single hit is present on either or both of the central pair of wires in the group, at least one of the check-sums shown in Table 5 can be formed by using three of the available hit times. In the Table the efficiency of an inner (outer) wire, from the group of four, is denoted by ε_{in} (ε_{out}).

The resulting distributions of the check-sum values have

Table 5
Efficiency check-sums using three hits

	Form	Wires hit				Probability
		1	2	3	4	
C_3	$T_2 - \frac{1}{3}(T_4 + 2T_1)$	1	1	1	1	$\varepsilon_{\text{in}}^2\varepsilon_{\text{out}}^2$
C_4	$T_2 - \frac{1}{3}(T_4 + 2T_3)$	1	1	0	1	$(1-\varepsilon_{\text{in}})\varepsilon_{\text{in}}\varepsilon_{\text{out}}^2$
C_5	$T_3 - \frac{1}{3}(T_1 + 2T_4)$	1	1	1	1	$\varepsilon_{\text{in}}^2\varepsilon_{\text{out}}^2$
C_6	$T_3 - \frac{1}{3}(T_1 + 2T_4)$	1	0	1	1	$(1-\varepsilon_{\text{in}})\varepsilon_{\text{in}}\varepsilon_{\text{out}}^2$

a clear double peak structure similar to that obtained from C_2. By fitting the area of the double peaks for each of the check-sums, background is excluded and an estimate of the relative probability for each of the four classes is obtained. These areas can then be combined to given an estimate of the efficiency of the central pair of sense wires:

$$\frac{\text{Area}\ (C_3 + C_5)}{\text{Area}\ (C_4 + C_6)} = \frac{\varepsilon_{\text{in}}}{(1-\varepsilon_{\text{in}})}, \tag{22}$$

thus providing a continuous monitor of the drift chamber efficiency. Fig. 26 shows the efficiency of the inner wires in the Planar and Radial drift chambers, obtained by the above method, for all 1993 and 1994 e–p runs (to 6/9/94). The decreasing trend, which is visible in both chambers throughout 1993 running, is due to leakage of N_2 into the system (about 1% by volume at run 53 000 to about 5% by volume at run 65 000). This fault was corrected for 1994 runs.

For the Planar chambers the figure shows that the inner wire efficiency is approximately 98% for the bulk of the 1994 data. The geometry of the cells is such that the pulse size is greater on the outer pair of wires thus giving a higher efficiency, leading to a mean over all four wires greater than 98%. The sharp drop in efficiency close to run 85 000 was caused by saturation of a gas purifier.

The efficiencies for the Radial chambers are averaged over three groups of four wires taken from the 12 wires in a drift volume. Nonuniformity in the electrostatics, particularly at the front of the drift chamber, leads to a lowering of efficiency on the front wires. The sharp changes in efficiency close to run 65 000 were due to a change in sense wire operating voltage, followed by a test period with a xenon gas mixture.

The check-sum method uses isolated hits; however additional inefficiencies arise with multiple hits because of overlapping. An estimate of the relative efficiencies of the

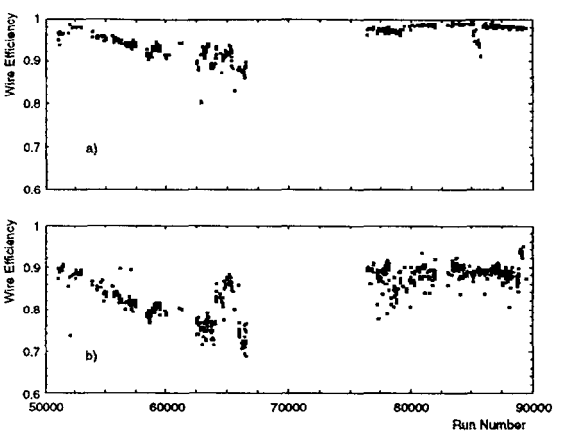

Fig. 26. Inner wire hit efficiencies for the Planar (a) and Radial (b) chambers.

different wire planes can be obtained by making a simple ratio of the number of hits found per wire relative to the wire with the most hits. This method gives an efficiency of 100% for the wire with most hits. For the planars the two methods are in reasonable agreement as the basic unit is a four wire group. For the radials there are 12 wires in a cell and the absolute measurement is performed independently for the front, middle and back four wires. The relative efficiencies have to be scaled by the absolute efficiency to arrive at efficiencies for all 12 wires. These wire efficiencies for 1993 and 1994 data are given in Table 6 and provide the input to the detector simulation (see Section 9.1).

4.6. Calibration in practice

The calibration principles described above have been applied according to the scheme outlined in Fig. 27.

H1 event data are transferred from the FTD front-end system into the Level 4 Filter Farm where the FADC data are processed by the QT algorithms (Section 3) to produce banks of Radial and Planar hits.

These QT banks are transmitted directly to the FTD on-line processing task running on the L4 farm, which generates the on-line histograms (drift time distributions, check-sum distributions) which are monitored in real time. At the end of each run the histograms are transferred to the DESY IBM mainframe where they are analysed to extract calibrated parameters which are accumulated in a history file. The history is inspected frequently by physicists who update the H1 data base with new calibration constants whenever a significant change is observed. This procedure is sufficient because of the stability of the FTD operating conditions (e.g. Section 4.2, Fig. 15).

Calibration constants for the Planar chambers are entirely determined in the above analysis of on-line histograms. In the case of the Radial chambers, where a direct on-line measure of drift velocity is more difficult and less accurate, the precision drift velocity obtained by projection of Planar track segments (Section 4.3.1; Fig. 21) is preferred even though the value for the current run is not immediately available for reconstruction purposes. In practice, this velocity varies sufficiently slowly that a weighted average taken from previous runs is in any case a more reliable

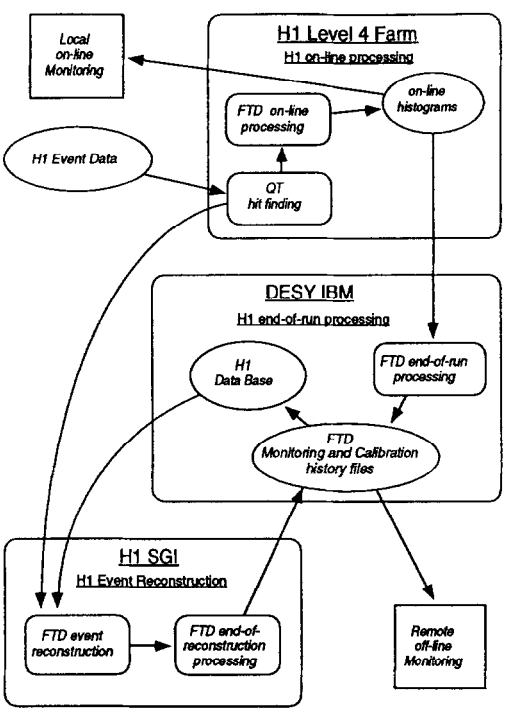

Fig. 27. Monitoring and calibration of the H1 Forward Tracker Chambers.

determination than the result based on a single run. The value obtained from the C_2 check-sum is still used as an important monitor and to detect significant discontinuous changes.

Constants from the H1 data-base and the QT banks from the L4 farm are passed to the H1 event reconstruction program, running on a Silicon Graphics (SGI) cluster. Output from this is analysed to derive updated drift velocities for the Radial chambers.

5. Line segment finding

Following the QT analysis of the FTD raw data and conversion of the resultant drift times to drift distances, the pattern recognition for the FTD starts by finding line segments independently in the Planar and Radial cham-

Table 6
Wire-by-wire single-hit efficiencies as used in the Monte Carlo simulation, derived from 1993 and 1994 data. The outer pair of Planar wires are assumed 100% efficient

	Wire											
	0	1	2	3	4	5	6	7	8	9	10	11
Radial 93	0.11	0.47	0.65	0.72	0.72	0.74	0.74	0.74	0.71	0.73	0.70	0.69
Radial 94	0.24	0.71	0.84	0.87	0.85	0.86	0.87	0.86	0.88	0.88	0.88	0.83
Planar 93	*1.00*	0.89	0.89	*1.00*								
Planar 94	*1.00*	0.98	0.98	*1.00*								

bers. Due to the different geometries of the chambers the procedures used are independent and are described separately in the two following Sections.

5.1. Line segment finding in the Planar chambers

5.1.1. Geometry

A charged track passing through an orientation will deposit charge, usually in one cell. In the good approximation that the path of the track through a cell is straight, the information from the drift distances to the four sense wires can be expressed as a plane (Fig. 28). This is also found to be the computationally most efficient way to treat this information. The Planar chambers are read out at only one end of the wires, so there is no knowledge of track position along the direction of the wire.

A track passing through a module is described by a plane from each of the X, U, and V orientations (Fig. 4). Clearly these three planes must intersect along the track within tolerances (Fig. 29).

With only one track through a module, and perfect measurement, pattern recognition would be trivial and completely defined by the observations above. However, in general, there are high track multiplicities in these chambers, and the main task of pattern recognition is to cope with the very high rates of hodoscope ambiguity this causes. There are two distinct stages to Planar pattern recognition: firstly clusters of three or four digitisations are found in individual orientations and then full line segments are constructed from these clusters for each module.

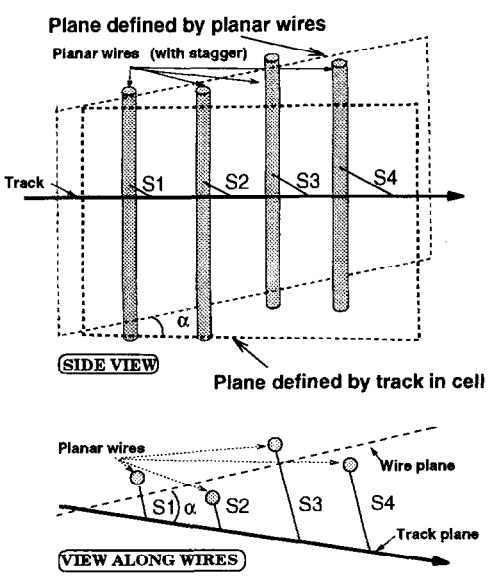

Fig. 28. The plane defined by a track passing through a cell (Fig. 5). α is the angle between wire plane and track plane, s_1, s_2, s_3, s_4 are the drift distances.

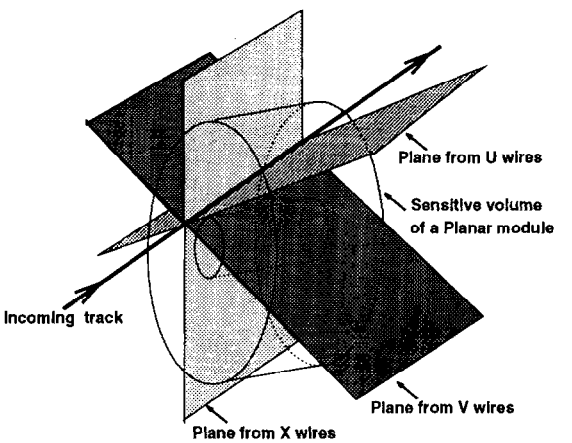

Fig. 29. Perspective view showing planes in which the track lies, as determined by the three orientations; their intersection gives the trajectory through the sensitive volume of a Planar module.

5.1.2. Stage 1: Finding clusters in an orientation

The distance between the first and last wires in an orientation is 1.8 cm. To a good approximation even particles of a few tens of MeV leave straight tracks on this scale. The first step is to find as many candidates for tracks within each orientation as possible. These candidates are referred to as clusters and define a plane as described above. Ionisation left by a particle gives two possible positions as there is no information about the direction from which it arrived at the wire. The false positions created by choosing the wrong drift sign are called reflections.

A number of searches is made. Data that have been used to form clusters are removed each time. On the first pass each hit, and its reflection, on the first wire plane in z is paired in turn with each hit on the last wire plane. A search is made on the two intermediate wire planes for any hits within four standard deviations of a straight line drawn between each pair. Clusters which have large angles to the beam direction, or position and angle correlations which are inconsistent with being a track from the e–p intersection point, are excluded. An example of finding clusters in this way is shown in Fig. 30.

In this example a small part of an orientation is shown with three tracks (A, B, C). The resulting digitisations are shown together with their reflections. The five clusters found using the above procedure are labelled. Possible clusters which failed to find hits on the inner wire planes are shown as dashed lines. Clusters which failed the angle cuts are not shown for reasons of clarity. The shaded area shows a case of two candidates within tolerance on the second plane. Both sets are recorded as clusters in this case. Even in this simple example false clusters have been recorded, and a method for removing them is required.

The set of clusters is now reduced until a subset is found that do not share any digitisations. The aim is to remove as

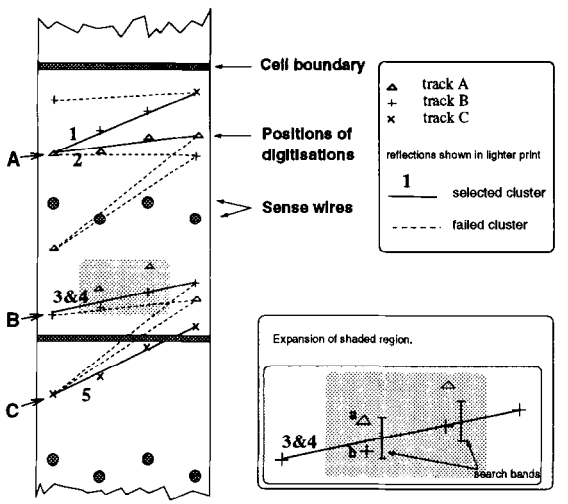

Fig. 30. View along the wires of part of an orientation showing the cluster finding techniques. In the expansion of the shaded region the bars indicate inner wire plane search regions. Candidate clusters are shown as lines joining the first and last digitisations. Clusters 3 and 4 are recorded as two separate clusters, one with digitisation "a" and the other with "b" on the second plane.

few clusters as possible to achieve this. There is no unique method, but the one described below has been found to work rapidly and with high accuracy and efficiency. It is useful to have a pictorial representation of the set of clusters as a network of nodes and arcs. Each node represents a cluster and an arc joins any two nodes that have at least one digitisation in common (see Fig. 31).

The node (cluster) with the largest number of connections is removed from the set. This is repeated until there are none with more than two connections. Apart from isolated nodes the only possible network topologies remaining are pairs of linked nodes or longer strings, and closed loops (Fig. 32). All clusters in loops are fitted to a straight line, as are clusters in the middle of strings, and the worst fitting candidate is removed. Clusters forming pairs are both fitted and the worse one removed. This algorithm avoids the need to perform a fit on all but a few of the clusters thus giving speed where the amounts of data are largest.

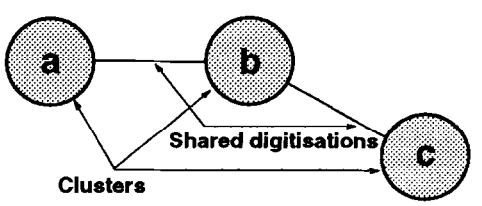

Fig. 31. The elements of a network description of the set of clusters and their relationships. Cluster "b" shares digitisations with clusters "a" and "c", but there is no sharing between "a" and "c".

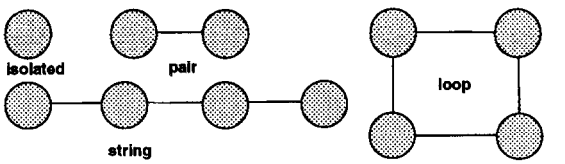

Fig. 32. The possible network topologies after nodes with more than two connections are removed.

This procedure is shown applied to the simple example presented earlier (Fig. 33). In this case the method takes two steps to produce a disconnected subset of clusters. Those chosen are the ones that relate to the tracks shown in Fig. 30.

Having found a disconnected subset of clusters in this way, another search is made. Data not already used in clusters forming the disconnected subset are searched again with more relaxed tolerances and with no cut requiring the clusters to point to the e–p interaction point. The method is repeated as before and the disconnected subset of clusters which it produces is added to the previous subset.

Because of inefficiencies, clusters may not have data on all four wires of the orientation. Therefore searches are made for three-hit clusters in the following order:

i) Clusters with one of the middle wire planes missing,
ii) Clusters with the first wire plane missing,
iii) Clusters with the last wire plane missing.

The tolerances used for clusters with three digitisations are always tighter than with four as the potential for random association is much greater. At each stage a second search is made with more relaxed tolerances; a new disconnected subset of clusters is formed and added to the existing subset. Any data remaining unused are fed to the next level.

It is found that approximately 70% of digitisations are used in the subset of disconnected clusters after a full search. The remaining 30% are due to track related noise arising, for example, from delta ray production.

5.1.3. Stage 2: Finding segments in a module

The input to this second and final stage of Planar pattern recognition is the disconnected set of clusters from the first. As explained above each cluster defines a plane (Fig. 28). If three of these planes, one from each orientation within a module, are from the same track they will share a common intersection within measurement tolerances (Fig. 29). To look for these signals the intersections between all pairs of planes are calculated. Any three such intersections which lie within a given distance of each other at the front and rear faces of the module indicate a line segment (Fig. 34). This distance cut (the segment cut) is currently 7 mm (see below).

Because of the large number of hodoscope ambiguities

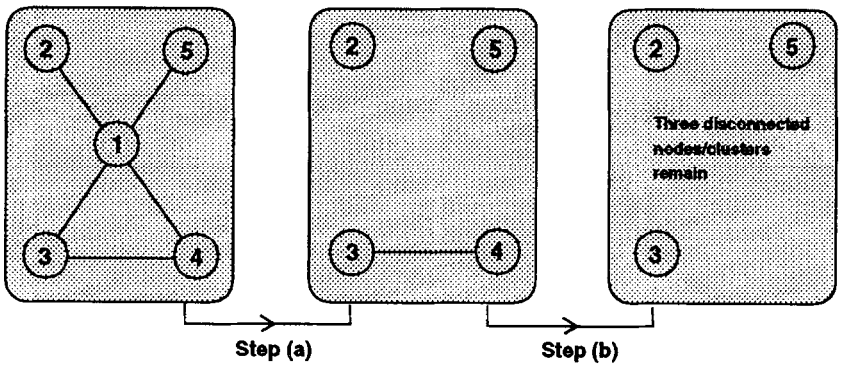

Fig. 33. An example of finding the disconnected subset of clusters for the case shown in Fig. 30. In step (a) the most highly connected node is removed, in step (b) the connected pair 3/4 is fitted and the worse removed.

even small numbers of tracks produce a large number of false line segments (Fig. 37 [I]). Most of these can be removed by selecting the subset of line segments that does not share digitisations.

The method chosen to achieve this can again be illustrated using a network of nodes and arcs. As before the method is not unique but has been found, from Monte Carlo studies, to select an almost complete set of correct line segments with few false segments for typical multiplicities (less than 20).

The digitisations belonging to each line segment are fitted to a straight line and the probability calculated. Each node (line segment) is given a weight which is the sum of the probabilities of all nodes connected to it (not including itself). The node with the highest number of connections is then removed. If this node is not unique then, of the nodes with the highest number of connections, the one with the highest weight is removed. This procedure is repeated until a disconnected set of nodes remains (i.e. no line segments share digitisations).

A simple example of this procedure is shown in Fig. 35. Initially there are nine connected nodes with fit probabilities and weights as shown in Fig. 35 (i). Nodes 4 and 6 both have five connections, but 6 has the highest weight (3.26) and is therefore removed (Fig. 35 (ii)). The node

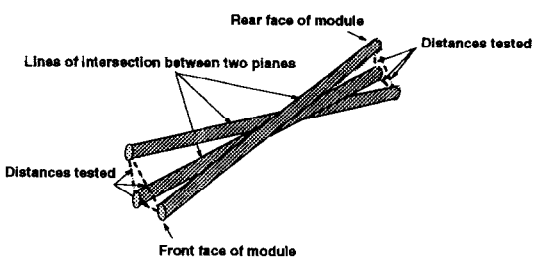

Fig. 34. Three intersections between pairs of planes. If all the distances represented by dashed lines are less than 7 mm then the three clusters/planes producing these intersections are selected as a line segment.

weights and connections must now be recalculated. Node 4 still has the highest number of connections and is now removed (Fig. 35 (iii)), followed by node 8 (Fig. 35 (iv)). Finally node 1 is removed, as it has the higher weight, and a disconnected set of segments is found.

This method used for segments is more elegant than that used for clusters and is possible because the smaller number of segments enables the algorithm to be more computationally intensive.

5.2. Performance of the Planar pattern recognition

The effectiveness of the method described was measured using a Monte Carlo simulation. Muon tracks were generated with 100% digitising efficiency which evenly populated the FTD in angle and with a flat momentum distribution between 0.5 and 50 GeV/c. A two-track resolution of 2 mm was assumed. The efficiency for finding good clusters is shown as a function of the number of tracks through the FTD (Fig. 36). The efficiency is above 95% even for 40 tracks (Fig. 36a); the number of losses and mistakes is small (Fig. 36b). The method for finding clusters will construct essentially all those which survive the intrinsic resolution for two tracks; however, many false ones are also created. This plot shows that it is possible to regain the correct sample by selecting a disconnected subset as described above.

The percentages of good segments in the total population of all found segments (a) and separately in the disconnected set (b) are shown in Fig. 37 [I] using a segment cut of 3 mm (see Fig. 34). A good segment is defined here as one which has at least 9 out of a potential 12 hits from the same Monte Carlo (genuine) track. This sample, however, predominantly consists of segments formed with 12 hits from the same track. The fraction of all segments formed which are good falls to 50% for 15 tracks and 20% for 40, but the proportion of good segments in the chosen disconnected subset stays at almost 100% for 20 tracks. By choosing a disconnected subset of the segments some of the good segments found are then

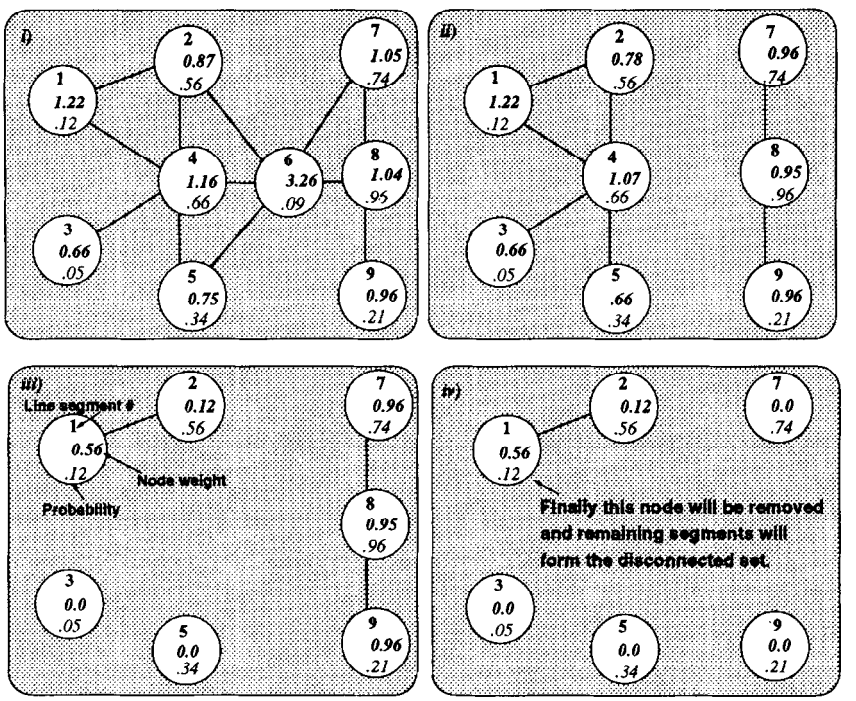

Fig. 35. The sequence (i) to (iv) shows how a disconnected set of line segments is obtained.

excluded, and this percentage is shown by the histogram (c). It is noted that this percentage matches very closely the percentage of false segments in the subset $((b)+(c)\approx 100\%)$. This shows that the disconnected subset contains approximately the true number of segments. Fig. 37 [II] shows the efficiency to find a genuine segment in the disconnected subset as a function of track multiplicity (a); also shown is the contamination (b). The subsequent analysis uses only segments in the disconnected subset.

In real data, because of problems beyond the intrinsic digitisation resolution, a segment cut of 7 mm is currently required, and the efficiencies for this value are shown in Fig. 37 [III] and [IV]. If the knowledge and the functioning of the chambers and associated electronics were perfect and given an intrinsic point resolution of ~200 μm, a cut of less than 3 mm could be used. It can be seen that going to the higher value cut causes a significant degradation.

For the majority of the data the probability of losing more than one hit per cluster is very small (see Table 6). However in a non-negligible number of cases there is a loss of more than one digitisation or even the correlated loss of a whole cluster (see Section 9.1). An extension to the segment finding method described above is therefore being developed. Segments are constructed from any unused data using two clusters confirmed by only one or two digitisations in the remaining orientation. A disconnected set of these is formed and added to the existing set. Finally, from any remaining data, segments are formed from two clusters alone and another disconnected set is added to the above.

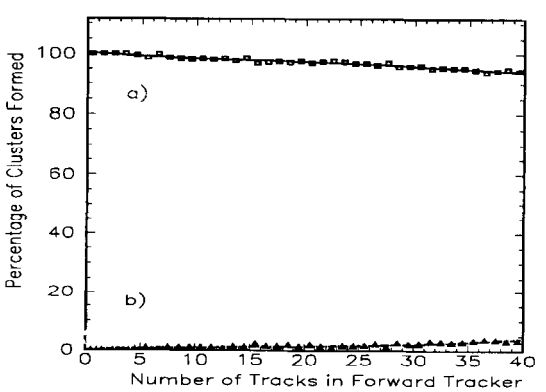

Fig. 36. Planar code performance as a function of track multiplicity: (a) 4-hit clusters formed with no mistakes and (b) 4-hit clusters with one mistake or 3-hit clusters with no mistakes.

5.3. Line segment finding in the Radial chambers

The procedure that has been adopted is to search for straight line segments in drift based on triplets of adjacent points. Line segment finding is carried out wedge by wedge. Within a wedge all triplets of digitisations are selected that satisfy the criterion

$$\left|\tfrac{1}{2}(d_1+d_3)-d_2\right|<P_1\,, \tag{23}$$

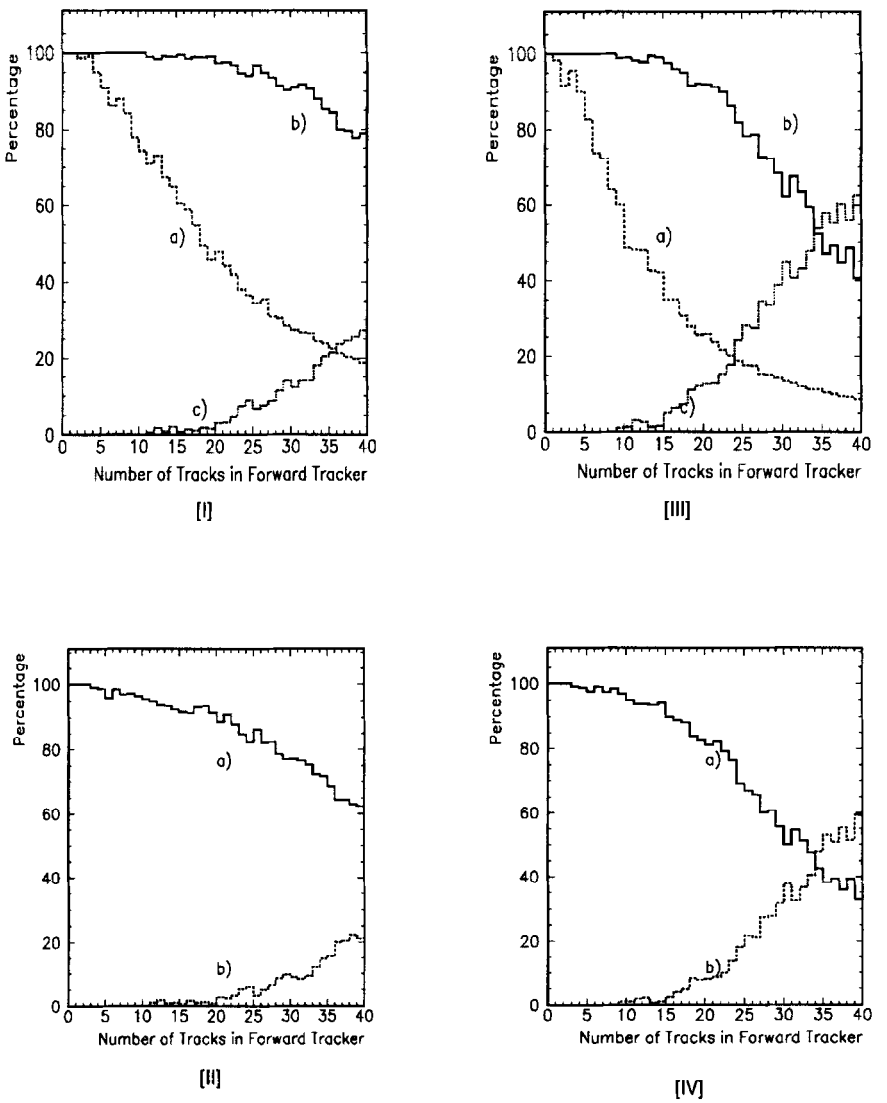

Fig. 37. Planar code performance as a function of track multiplicity: [I] (a) percentage of all segments which are good, (b) percentage of segments in the disconnected set which are good and (c) percentage of good segments lost by choosing the disconnected set. [II] (a) percentage of genuine track segments found in the disconnected set and (b) percentage of segments which are not good (see text). [III] and [IV] are the same as [I] and [II] but with a 7 mm rather than a 3 mm segment cut.

where d_1, d_2, d_3 are signed distances to the wire plane and P_1 is a parameter (approximately 1 mm).

For the majority of triplets, this resolves the left–right ambiguity of the three points and gives the sign of the drift. The next step is to join the triplets. This is done if triplets have points in common with the same drift sign, and the resultant group of hits lies within a certain tolerance of a straight line joining the first and last points of the group. If triplets are separated by one missing digitisation, they may also be associated if they satisfy this straight line criterion. The associated triplets are then fitted to a straight line. The parameters of this fit are used to project along the wedge and associate isolated digitisations with the joined triplets. At this point there is a set of potential line segments of which the best is selected, either as that line segment with the maximum number of points or, if the two longest segments have the same number of points, that with the best χ^2 to a straight line. The points making up the line segment are marked used, the points are recorded and the program returns to re-examine remaining points in the wedge or transfers to the next wedge if insufficient digitisations remain to form a line segment.

The procedure described above finds points belonging to a track segment provided that it lies entirely within one Radial wedge. In practice, this may not be true. Since

tracks are, to a good approximation, straight lines in ϕ–z line segments can be extrapolated in ϕ into nearby wedges to pick up associated digitisations.

6. Line segment linking

6.1. The track model

The line segments forming a track lie on a helix. A helix fit could be used to check if a set of line segments is consistent with belonging to a track, but this would be prohibitively expensive in computer time. Consequently an approximate track model is used to represent a helix and this track model is used to link line segments and to verify that the line segments are consistent with lying on a helix.

With the definitions:

$$\tan(\hat{\phi}) = \frac{(y - y_v)}{(x - x_v)} \tag{24}$$

$$\hat{R} = ((x - x_v)^2 + (y - y_v)^2)^{1/2} \tag{25}$$

where x, y are the coordinates of a point on a track, and with θ as the polar angle of the track with respect to the z-axis, the helical trajectory of a particle, momentum P, charge Q, passing through the known point x_v, y_v, z_v, is given by

$$\hat{\phi} = \hat{\phi}' z + \hat{\phi}_0 \tag{26}$$

$$\hat{R}(z) = \frac{\tan(\theta)\sin(\hat{\phi}'(z - z_v))}{\hat{\phi}'} \tag{27}$$

where $\hat{\phi}' = (KP\cos(\theta))^{-1}$, $K = -2/BQc$, B is the magnetic field (along z-axis) and c is the velocity of light.

For tracks that have originated close to the z-axis ($x_v = y_v = 0$), e.g. tracks from the primary vertex, it follows from Eqs. (26) and (27) that a good track model is

$$\phi(z) = \phi' z + \phi_0 \tag{28}$$

irrespective of momentum, and provided that ϕ' is small (i.e. high momentum) then

$$R(z) = R' z + R_0 \tag{29}$$

where $\tan(\phi) = y/x$ and $R = \{x^2 + y^2\}^{1/2}$. Thus the helix is approximated by straight lines in ϕ–z and R–z. For off-axis tracks, the ϕ–z relation is well approximated by a parabola; the R–z relation becomes parabolic both for off-axis tracks and for low momenta. These representations allow the Planar and Radial chambers to be treated in an identical manner.

The coordinate W (Fig. 38) is given by $W = y\cos(\alpha) - x\sin(\alpha)$, where α is the azimuthal angle of the Planar or Radial wire. If a track model has been defined in $\hat{\phi}$–z and $\hat{R}$–z, the coordinate, $W(z)$, at a given z is given by

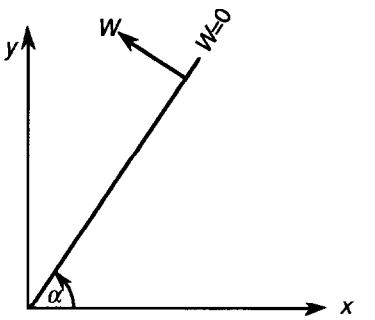

Fig. 38. The coordinate W measured by sense wires at an angle α.

$$W(z) = \hat{R}(z)\sin(\hat{\phi}(z) - \alpha) + y_v\cos(\alpha) - x_v\sin(\alpha). \tag{30}$$

Thus a χ^2 evaluated in drift can be used to determine whether the track model is consistent with the measured drifts and hence verify that the line segments are correctly linked. Note that while Eqs. (28) and (29) are adequate representations for a track through the Radial chambers (due to the small values of $\phi - \alpha$), it is essential to use Eq. (27) or a parabolic relation in R–z if Eq. (30) is used for the Planar chambers.

There are four steps in the linking of segments to form tracks: firstly, the line segments found in the Planar chambers are joined to form potential tracks and these tracks are in turn linked to Radial line segments. Secondly, and independently, Radial segments are linked to form tracks that are in turn linked to Planar line segments. Due to chamber inefficiencies and two-track resolution neither procedure finds all tracks, so in a third step the tracks found in the first two steps are compared and the best selected. In a final step unlinked Planar segments are joined to unlinked Radial segments where possible. The following three Sections describe these procedures in detail.

6.2. Track finding using the Planar line segments

The Planar line segments are fitted to straight lines in x–z and y–z. These parameterisations are readily converted to ϕ and R so that the approximate helix representations of Section 6.1 can be used to verify the linkage of Planar segments.

The first operation is to join the Planar line segments to form tracks. This is done pair-wise by projecting the segments to a plane midway between them. For high momentum tracks the pitch of the track helix is much greater than the separation of the planar modules, so these segment projections to the midplane have approximately the same x, y (within 1 mm for tracks of momentum greater than 0.5 GeV/c). Line segments are linked to form a track if $D = (x_1 - x_2)^2 + (y_1 - y_2)^2 < D_{\max}$, where x_1, y_1 (x_2, y_2) are the coordinates of the projections of line segments 1(2) and $D_{\max}$ is a parameter presently set to

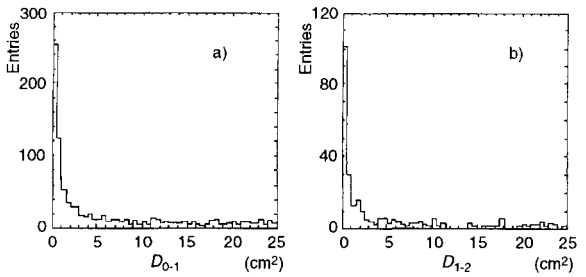

Fig. 39. The distribution of the parameter D used to link Planar line segments, (a) linking 0–1, (b) linking 1–2 for three-module tracks.

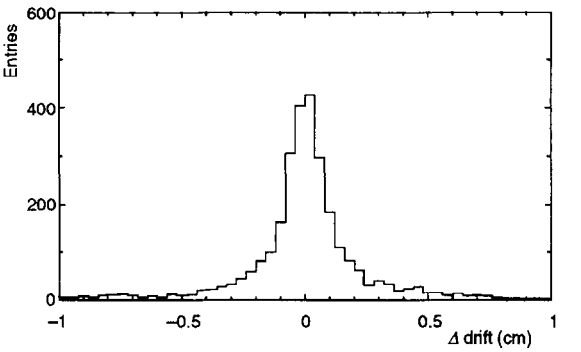

Fig. 40. The distribution of predicted drift minus measured drift, Δ drift, for Radial line segments associated with Planar based tracks.

5 cm^2. The Planar line segments are sufficiently well defined that it is clear from histograms of D (see Fig. 39) that little random linkage occurs (a few percent only). In the linking an hierarchical approach is followed; the linking procedure is applied first to form three-module tracks, then to form two-module tracks from those segments that do not form three-module tracks. For the two-module tracks adjacent modules are linked first. A χ^2 in drift is determined based on parabolae in ϕ–z, R–z and Eq. (30) for three-module tracks, and on Eqs. (24), (25), (26), (29) and (30) for two-module tracks. These χ^2 are used to reject bad links and to select the best links if ambiguities exist.

Following the linking of the Planar segments, the track candidates are parametrised by fitting the segments to straight lines in ϕ–z and R–z, so defining approximate helices. Having parametrised the Planar tracks in this manner it is possible to associate Radial line segments with the Planar tracks. This is done in two steps. Firstly, the mean Radial drift is compared with that predicted from the Planar track using

$$W = R(z)\sin(\phi(z) - \alpha)\,, \tag{31}$$

with R and ϕ from straight line fits to the Planars. Secondly, the slope of the Radial line segment, dW/dz, is compared to that expected from Eq. (31). If the Radial segment is within some tolerance of the prediction it is associated with the Planar track. The distribution of measured drift minus predicted drift for associated Radial line segments is shown in Fig. 40, from which it can be seen that there is little evidence for misassociation.

6.3. Track finding using the Radial line segments

The digitisations associated with the Radial based line segments are first converted to ϕ using

$$\phi = \tan^{-1}(W/\mathcal{R}) + \alpha\,, \tag{32}$$

where $\mathcal{R}$ is the mean radius of the digitisations weighted by the error in R estimated from the magnitude of the integrated charge. Note that the error in ϕ is dominated by that in $\mathcal{R}$. A straight line fit in ϕ–z is made for each segment.

Firstly an attempt is made to make three-module links. Potential candidates to form a track are required to lie in a straight line in R–z to a tolerance of about 10 cm. Since in ϕ–z the line segments lie either on a straight line or a parabola, the line segments are projected in ϕ–z to a plane midway between adjacent modules and the projected ϕ–z values are required to agree within about 0.05 radian. This value is required to take account of bad radius measurements in regions of high track density. Fig. 41 shows the difference in ϕ at midplane. A clear peak is evident, demonstrating segment linking with a low level of misassociation, especially for three-module tracks (Fig. 41b). A final check is that the line segments lie in an approximate straight line in ϕ–z. These potential three-module tracks are next subjected to more stringent tests. A weighted least squares straight line fit in R–z is made to all points forming the track. For each digitisation an improved value of ϕ is determined using R from this fit. A parabola in ϕ–z together with the fit in R–z is used in Eq. (30) (with $x_v = y_v = 0$) to determine a χ^2 for the track. A check is also made that the slope of the line segment, dW/dz, agrees with that from Eq. (30); this verifies that the momentum from each line segment agrees with that from the overall track model. Tracks are rejected if the χ^2 is too large or if dW/dz differs from that predicted by more than some empirically determined tolerance. At this stage several line segments could be shared amongst different tracks. Tracks are compared on the basis of χ^2 and, if two share the same line segment, that with the lowest χ^2 is retained. After this selection, line segments that have formed three-module tracks are marked used and the program goes on to search for two-module tracks in the unused line segments.

In this second stage a search is made for two-module tracks in the sequence 0–1, 1–2, 0–2. Line segments are marked used after each level of two-module pattern

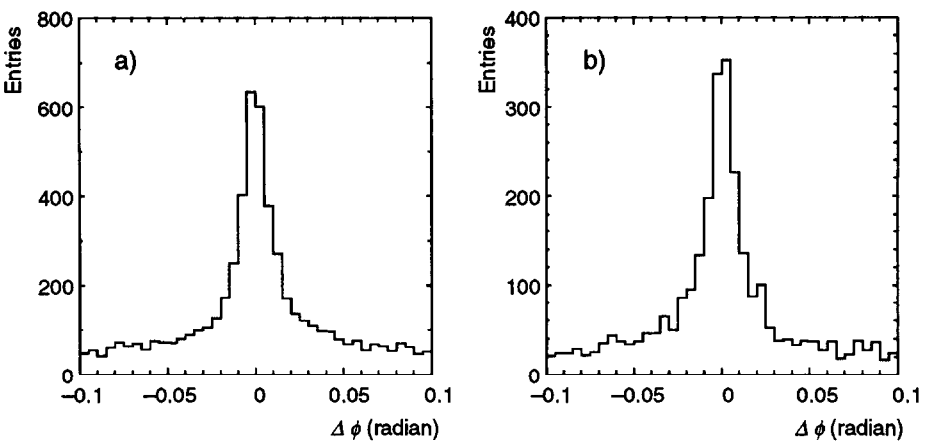

Fig. 41. Difference in ϕ, $\Delta\phi$, at the midplane between (a) Radials 0 and 1, and (b) Radials 1 and 2 for three-module tracks.

recognition. The criteria for deciding what is a good track candidate follow closely the procedure for three-module tracks except that there are no initial checks for straight lines in ϕ–z, R–z; the only requirement is that the projected ϕs agree at the midplane within tolerance. A final χ^2 is determined using Eqs. (24)–(26), (29) and (30) with x_v, y_v being the first point on the track. Also dW/dz is compared with the expectation from the track model. Potential tracks are accepted if χ^2 and dW/dz are within tolerance. As in the case of the three-module tracks, tracks with common line segments are compared and that with the lowest χ^2 retained.

In the final stage of the Radial based pattern recognition, the tracks found in the Radial chambers are associated with line segments in the Planar chambers. Straight lines in ϕ–z and R–z are used for both interpolation and projection. The projection in ϕ, which is equivalent to a projection in drift, is more accurate than that in radius, and consequently the quantity $(\phi_p - \phi_r)R_p$, where ϕ_p, R_p are the mean ϕ and radius of a Planar line segment and ϕ_r is the ϕ predicted by the Radial based track, is used to select the Planar line segments.

6.4. Track selection and linking of single Planar line segments with Radial line segments

At this stage in the pattern recognition there are three- and two-module Planar based tracks that have been linked to Radial line segments where possible, plus an independent set of three- and two-module Radial based tracks with associated Planar line segments. A unique set of three- and two-module tracks is now selected. The selection procedure depends on the efficiency of the hardware. At present Planar based tracks are favoured over Radial based tracks and a Radial based track is retained only if it is verified by at least one Planar line segment. After this selection there remain unassociated single Planar and Radial line segments. In the final stage of pattern recognition the single Planar line segments are fitted to straight lines in ϕ–z and R–z and these lines are extrapolated into the Radial chambers. An association with the Radial chambers using Eq. (31) is made as before but with somewhat larger tolerances.

There remain single Planar segments unassociated with either Radial or other Planar segments. Scanning of events indicates that most of these are part of good tracks, the remainder of the track having been lost due to chamber inefficiency, track overlap etc. Consequently they are retained and output as tracks. Single Radial line segments are discarded as they cannot be associated with a vertex due to lack of definition in R–z.

7. Track fitting using a Kalman filter

Following pattern recognition a Kalman filtering technique is used to determine the optimum track parameters [14]. Kalman filtering uses an incremental approach to fitting, whereby measurements are added successively to an initial set of track parameters (''state vector''). The state vector and its covariance matrix are projected successively to each measurement surface, with the effects of multiple Coulomb scattering added to the covariance. If a measurement exists at that surface the state vector is updated by forming a weighted mean with the measurement (known as filtering). When all measurements have been included an optimal estimate of the track parameters is obtained at the final surface, equivalent to a linear least-squares fit. A smoothing process is then applied to transform this optimal state vector back to the beginning of the track (and to all intermediate surfaces); in the absence of multiple scattering this is simply a helix extrapolation, but with multiple scattering the smoothed state vector tends to follow the true trajectory. A detailed description of the Kalman filter algorithm as implemented for the H1 Forward Tracker can be found in Section 7.4.

The Kalman filter is essential in an environment where multiple Coulomb scattering is significant. The H1 Forward Tracker contains approximately 0.5 radiation lengths of material, and this is distributed fairly uniformly, precluding the possibility of fitting the track in sections with scattering allowed between the sections (as is done, for example, in the H1 Central Tracker [15]). Multiple scattering can give a deviation of several centimetres over the length of the Tracker for low momentum tracks, and is therefore an important effect.

In a conventional least-squares fit multiple scattering is incorporated by fixing the track parameters at one point, typically the beginning of the track, and then increasing the errors at each subsequent point to reflect the cumulative amount of scattering along the track. However, these pseudo-errors are correlated, since they reflect the deviation of the true track from the track model. The track fit therefore requires the inversion of an $n \times n$ covariance matrix, where n is the number of measurements (up to 72 in this case). This is not necessary for the Kalman filter which follows the true track, with optimal parameter estimation at every measurement surface.

7.1. Choice of the track model

The representation of the state vector is chosen to given an approximately linear track model, because the Kalman filter uses a linear approximation for error propagation. It is also convenient to have a track model with as many vanishing derivatives in the Jacobian matrix F_k (Eq. (33)) as possible, as this allows considerable savings in computing time for the matrix algebra involved. The geometry of the Forward Tracker is particularly convenient in this respect. Since the magnetic field is uniform to better than 2% over the Tracker volume and parallel to the z axis the equation of motion is close to a helix, which gives a simple propagation from one z plane to another.

The representation used is $(x, y, q/p, \tan\theta, \phi; z)$ (i.e. z is fixed for each measurement surface), with the direction of the momentum vector, $\boldsymbol{p}$, defined by θ and ϕ in spherical polar coordinates. The main nonlinearity is in the dependence of x and y on ϕ; θ and q/p are constants of the motion, and ϕ increases linearly with z, proportional to $q/(p\cos\theta)$. First-order corrections to the track model are made for components of the field transverse to the z axis and for changes in the field as a function of position, but it is not necessary to include these effects in the calculation of the Jacobian F_k.

7.2. Point rejection

In a conventional fit it can be difficult to identify points which do not belong to the track, because any deviations become masked by multiple scattering, which can be much larger than the resolution on the points. With a Kalman filter this masking does not happen, and in addition measurements can easily be added or removed during the fitting process without refitting the entire track each time.

The mechanism for the addition of a new point during smoothing is simply to take a weighted mean of the measurement with the smoothed vector. To remove a point requires the inverse of this process, which is equivalent to the standard filter with a negative measurement covariance. After either of these the filtered and smoothed vectors at planes before this point are incorrect, but smoothing can continue with the new state vector without updating these. If the vector is only required at one end of the detector no more need be done, but otherwise it is necessary to restart the filter from the first altered point, and smooth back to this point. Further points may be added or removed in this process, and the procedure can then be iterated.

This facility is not a substitute for good pattern recognition. Although the Kalman filter can reject points which do not belong to the track this relies on the fitted track being a good approximation to the true track. The pattern recognition should provide a list of points and a state vector which, when extrapolated, goes within a reasonable distance (typically a few millimetres) of the points.

7.3. Removal of the initial state vector

The Kalman filter requires a "starting vector", which has to be provided by the pattern recognition. Ideally this should be assigned large errors to avoid biasing the fit, but in practice a compromise must be made. The reason for this is that the Kalman filter uses linear error propagation, and therefore the state vector must be kept sufficiently close to the true track that a linear approximation is acceptable (i.e. a first order Taylor expansion of the track propagation equation (Eq. (34)) about the fitted state vector should be an acceptable approximation). In practice assignment of errors to the starting vector which are about an order of magnitude larger than those expected after the fit gives little bias while maintaining the stability of the fit.

If necessary it is possible to remove the influence of the starting vector by treating it as a virtual measurement that can be removed as described in the previous Section. In the simplest case, having filtered from the start of the Tracker to the end and smoothed back to the start, the initial vector can be removed to give an unbiased result. However, this does not update the results at other planes, and the smoother is not reversible as is obvious from Eq. (34). A more sophisticated procedure is therefore needed if the unbiased result is required at more than just one end of the detector. This is achieved by starting the filter at a point part way along a track, and processing it in two sections. The filter first runs over one part and then smoothes back to the starting plane. The initial state vector is then removed, giving a state vector which contains information from the first section of the track. This is then projected into the other section, where it acts as a new initial state vector. Filtering and smoothing then proceed in the reverse

direction in that section. At this point the smoothed vector contains the full information from all measurements, with no influence from the initial state vector. The starting vector at that point is then removed, giving a vector with information from the second part of the track only. This is then projected back to the first section, and the filter/smoother is re-run over this section. This gives the desired result of a state vector at all points with the information from all measurements, but without any influence from the starting vector and without having to process the whole track twice.

7.4. Technical description

The general principles of Kalman filtering as applied to track fitting are given in Ref. [14], and the notation of that paper will be followed here. More details, applying in particular to the context of the DELPHI experiment, can be found in Ref. [16]. However, the expressions published in the above papers have been reformulated to optimise computing efficiency, stability and clarity. This reformulation, as described below, is in some cases completely general and in others depends upon specific properties of the H1 FTD, but has been found essential in order to achieve the reliability and speed required by mass-production event reconstruction.

A state vector (with 5 dimensions for a track fit) is written as x_k^i (lower case variables denote vectors, and upper case denotes a matrix), where k is the surface (plane) index and the value incorporates information up to plane i. The usual cases are x_k^{k-1} (or x_{k-1}^k) for a projected vector, x_k^k for a filtered vector and x_k^n for a smoothed vector (n is the total number of measurements). The covariance of x is similarly written as C_k^i. In the following x_k^k and C_k^k are written as x_k and C_k, respectively. The track model (which projects a state vector from k to $k+1$) is given by a function $f_k(x_k)$, and F_k is the Jacobian matrix:

$$F_k = \frac{\partial f_k}{\partial x_k} \equiv \frac{\partial x_{k+1}^k}{\partial x_k}, \tag{33}$$

where the derivatives are evaluated at x_k. Measurements are related to the state vector via $m_k = H_k x_k$ (where the dimensions of m_k and x_k are generally different). The measurement covariance is denoted by $V_k \equiv G_k^{-1}$, and the additional covariance on the state vector due to multiple scattering between planes k and $k+1$ by Q_k.

The three main steps are projection, filtering and smoothing. These are given in Ref. [14] as follows:

$$\begin{aligned} x_{k+1}^k &= f_k(x_k) \\ C_{k+1}^k &= F_k C_k F_k^T + Q_k ; \qquad \text{(projection)} \\ x_k &= C_k[(C_k^{k-1})^{-1} x_k^{k-1} + H_k^T G_k m_k] \\ C_k &= [(C_k^{k-1})^{-1} + H_k^T G_k H_k]^{-1} ; \qquad \text{(filtering)} \\ x_k^n &= x_k + A_k(x_{k+1}^n - x_{k+1}^k) \\ C_k^n &= C_k + A_k(C_{k+1}^n - C_{k+1}^k)A_k^T \\ A_k &= C_k F_k^T (C_{k+1}^k)^{-1} . \qquad \text{(smoothing)} \end{aligned} \tag{34}$$

The projection step is straightforward; application of the track model to x, and linear error propagation for C. The filtering step is also simple, being a weighted mean of the projected vector with the measurement. However, the formulation given above contains two inversions of 5×5 matrices, and this can be simplified:

$$\begin{aligned} x_k &= [1 + C_k^{k-1} H_k^T G_k H_k]^{-1} x_k^{k-1} + C_k H_k^T G_k m_k \\ C_k &= [1 + C_k^{k-1} H_k^T G_k H_k]^{-1} C_k^{k-1} \end{aligned} \tag{35}$$

which only involves one inversion. Also, the expression for x_k is of the form

$$x_k = W_1 x_k^{k-1} + W_2 H_k^T m_k , \tag{36}$$

where the weight matrices W_1 and W_2 (with $W_2 = C_k H_k^T G_k H_k$) satisfy $W_1 + W_2 = 1$; Eq. (36) can therefore be re-expressed as

$$x_k = H_k^T m_k + W_1(x_k^{k-1} - H_k^T m_k) , \tag{37}$$

which reduces the number of matrix multiplications.

Another major improvement can be made to the filter equations. The measurements are always space points, and the measurement covariance is therefore 2×2 in general (even for Planars the matrix will effectively be 2×2 after rotation into (x, y) space, unless the wire is along the x or y axis). The matrix to be inverted is therefore much simpler than a general 5×5 matrix, and can be inverted analytically (it has two columns of arbitrary elements, with the remaining diagonal elements being unity and other elements zero).

A further improvement can be obtained for Planars by factorising the transformation matrix H out of the inversion. Define H' as the equivalent 5×5 rotation matrix:

$$H' = \begin{pmatrix} -\sin\phi & \cos\phi & 0 & 0 & 0 \\ \cos\phi & \sin\phi & 0 & 0 & 0 \\ 0 & 0 & 1 & 0 & 0 \\ 0 & 0 & 0 & 1 & 0 \\ 0 & 0 & 0 & 0 & 1 \end{pmatrix} . \tag{38}$$

Then,

$$C_k = H_k' {}^T [1 + H_k' C_k^{k-1} H_k' {}^T G_k']^{-1} H_k' C_k^{k-1} , \tag{39}$$

where G_k' is a 5×5 matrix with the inverse of the measurement error in the $(1, 1)$ element, and zero elsewhere. The matrix to be inverted then has one column of arbitrary elements, unit diagonal elements elsewhere and is zero otherwise, and is consequently easy to invert.

The smoothing equations given above are not transpar-

ent, and can be improved in both clarity and efficiency. Some manipulation gives the equivalent formulation

$$\begin{aligned} x_k^n &= f_k^{-1}(x_{k+1}^n + W_k[x_{k+1}^k - x_{k+1}^n]) \\ C_k^n &= A_k C_{k+1}^n A_k^T + C_k(1 - F_k^T A_k^T) \\ &= A_k C_{k+1}^n A_k^T + C_k F_k^T W_k^T F_k^{-1T} \\ &= A_k C_{k+1}^n A_k^T + F_k^{-1} Q_k A_k^T \end{aligned} \tag{40}$$

where $A_k = F_k^{-1}(1 - W_k)$ and $W_k = Q_k(C_{k+1}^k)^{-1}$.

In the first line, F_k^{-1} has been replaced by f_k^{-1}, which is the full inverse track transformation, rather than a linearised approximation; this gives a much better behaviour for the smoother. The weight matrix W_k is essentially the ratio of the multiple scattering error to the total projected error, and is therefore zero if there is no multiple scattering. In this case, smoothing is just equivalent to a reverse helix transformation. In the presence of multiple scattering, the effect is to adjust the smoothed state vector at $k+1$ by the difference between the projected and smoothed vectors at $k+1$, weighted by W_k, which gives an estimate of the amount by which the track actually scattered between k and $k+1$. This adjusted vector is then projected back using the inverse transformation.

The expressions for the smoothed covariance are somewhat less transparent. In the absence of multiple scattering this again reduces to linear error propagation. The equivalent expressions given have a somewhat different behaviour, in that the second term of the second and third expressions manifestly vanishes as $Q_k \to 0$, whereas that in the first expression relies on a cancellation. The third expression is the one currently implemented, as it involves fewer matrix multiplications. It is, however, not evidently well-behaved if the multiple scattering is large, since the covariance should tend towards C_k, and this relies on a complex cancellation. This behaviour is possessed explicitly by the first two expressions. This would suggest that the second expression may be preferable in spite of the additional computation, and this question may require further investigation.

A further issue is whether F_k in the smoother (Eq. (40)) should be the same as that used in projection, or re-evaluated at the smoothed point. The most natural solution would appear to be the latter. In any case, in expressions involving both F_k and F_k^{-1} these must be exact inverses to give the correct asymptotic behaviour, and an extra matrix inversion is therefore required. This again indicates the use of the third of the above expressions for the smoothed covariance, as it only involves F_k^{-1} which is readily available from the inverse track transformation applied to the smoothed state vector. Conversely Q_k is not re-evaluated from the smoothed state vector, as the weight matrix W_k compares Q_k with the projected covariance, which includes multiple scattering calculated from the projected vector.

It should be noted that a matrix inversion is now only required if there is multiple scattering, and there is generally a large computational saving if multiple scattering can be neglected between any two planes.

7.5. Code optimisation

Various techniques have been used to increase the execution speed of the code. The two main methods are the expansion of matrix multiplication in-line and the use of the known properties of various matrices. These include the symmetry of covariance matrices, that multiple scattering does not change q/p, that the Jacobian matrix F_k has unit diagonal elements, that q/p and θ are constants of the motion and that changes in the momentum vector direction are independent of small changes in position. The latter two assumptions are true only if deviations from the nominal magnetic field can be neglected over each step of the Kalman filter, but this is a reasonable assumption.

For track extrapolation the track model is approximated wherever possible, either with a straight line or with first-order approximations for changes in angle. Small-angle approximations are also made where possible for the evaluation of trigonometric functions. Multiple scattering is neglected within a drift cell, as it entails a substantial amount of calculation.

This optimisation process has been essential to allow the Kalman filter technique to be used; the cumulative effect of all optimisations is to decrease the computing time needed by roughly two order of magnitude from a straightforward implementation, to a point where the Kalman filter accounts for about 20% of the computing time taken by the Forward Tracker reconstruction. After optimisation most time is spend in the projection of the state vector from one plane to the next, and the time is therefore roughly proportional to the number of measurements.

The increase in time if point rejection is used is unpredictable. The time to remove each point is negligible, but it is then necessary to perform another iteration of the whole fit for those planes which need updating; this time is independent of the number of points removed, but depends on the position of the last point removed, since points before this do not need to be updated. On average this results in about a 50% increase in computing time.

The main time overhead for the removal of the initial state vector is that the first part of the Tracker is filtered and smoothed twice. It is therefore desirable to have this section as small as possible. The main constraint is that after the removal of the initial vector, enough measurements must have been added to give errors sufficiently small that the filter remains stable. If points are added or rejected in the second pass over the first section this invalidates the result in the other section, so this has to be repeated.

8. Alignment of the Forward Tracker

8.1. Data sample

The internal alignment of the Forward Track Detector uses a sample of cosmic ray tracks recorded in zero magnetic field. These tracks were selected using a scintillator trigger that required the track to intersect the interaction region and to traverse all three Supermodules. Data are corrected for the time offsets measured for each individual cell using artificially generated test pulses. A special form of pattern recognition has been developed which exploits the fact that the tracks are straight lines.

8.2. Planar pattern recognition for alignment data

The nomenclature used in this Section is the same as that in Section 6.2. The four digitisations which form the best straight line for each orientation are found. All such digitisations (up to 36) are then fitted to a straight line. There are many occasions where track related noise and the intrinsic resolution of the data cause wrong digitisations to be chosen. A procedure for removing bad digitisations and adding in good ones is therefore implemented. Any of the digitisations contributing more than 100 to χ^2 or more than three and a half times the average χ^2/degree-of-freedom are noted. The worst two of these are removed from the track and the track is refitted. At wire planes which do not have a hit associated with the track the closest hit is attached if it is within a given distance of the track. The tracks are then refitted to give new track parameters and the procedure repeated until no further hits are removed or added. Checks are made to ensure the procedure does not loop; if it does the iteration is terminated. Scanning has verified that this method is efficient at correctly identifying hits and tracks.

This sample of tracks must however be treated with some caution as low momentum tracks have noticeable effects from multiple scattering. This causes them to have either a poor fit or few digitisations associated. To ensure a good sample, tracks are required to have an associated planar digitisation on at least 20 of the 36 planes and a $\chi^2 < 700$. Each event has also been scanned to ensure that the track is a sensible candidate. Given these requirements a sample of just over 500 clean tracks remains.

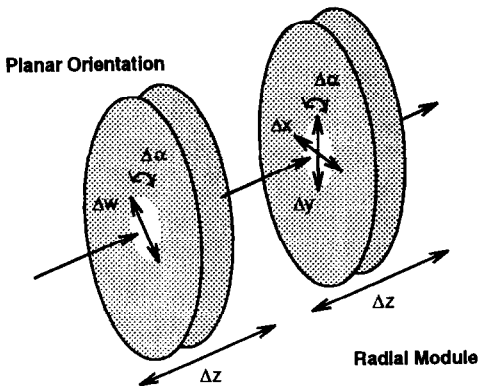

Fig. 42. Definition of alignment parameters relative to the nominal values.

8.3. Alignment of the Planar chambers

Tracks which satisfy the above criteria are corrected for the following.

- Time of flight. A correction is made to the drift time at each plane using the fitted track parameters and assuming the particle is travelling at the speed of light in the direction giving the smaller χ^2.
- Track angle effect. This is calculated from the fitted track parameters. The correction described in Section 4.1 is parametrised by a single variable d. The fitted value of d agrees well with that obtained from theoretical calculations (~0.5 cm).
- Propagation time along a sense wire. The propagation speed is fitted and found to be close to the speed of light.

Having made these individual corrections for each track a χ^2 is calculated for a global fit to all tracks. Before freeing the alignment parameters a global t_0 and drift velocity are fitted. Two additional parameters are fitted which describe any deviation from the nominal wire stagger and wire spacing within a cell. In the fit one orientation is fixed in space and each of the remaining eight orientations has Δz, $\Delta\alpha$ and ΔW fitted (see Fig. 42) where Δz is a translation along the z axis, $\Delta\alpha$ is a rotation about the z axis and ΔW is a translation perpendicular to the wires. The W coordinate of an extra orientation is fixed in order to uniquely specify the position of the FTD. The

Table 7
Planar alignment parameters with orientation 3 and the W coordinate of orientation 8 fixed at their nominal values, together with an estimate of the errors

	Orientation									Error
	0	1	2	3	4	5	6	7	8	
$\Delta\alpha$ [mrad]	−0.37	−0.29	0.13	*0*	0.15	0.10	0.08	0.10	0.16	0.15
ΔW [μm]	−8	55	57	*0*	102	−102	106	15	*0*	50
Δz [μm]	628	416	518	*0*	−751	207	−167	−192	28	500

results have been tested for stability by changing the orientation that is fixed and are given, along with an estimate of the errors, in Table 7. None of the resulting corrections have a significant effect on the track reconstruction with the exception of the rotation of orientations 0 and 1.

8.4. Alignment of the Radial chambers

The next step is to align the Radial chambers with respect to the Planar chambers. Digitisations from the Radial chambers are parametrised by their drift distance and the wire-angle in the x–y plane, ignoring any information from charge division. This makes Radial data similar to Planar data, with each Radial digitisation defining a line in space. The digitisations closest to the track defined by the Planars and within 0.5 cm of it are associated with the track. As it is not possible to determine the Radial drift velocity and t_0 using Radial data alone, a fit for these parameters is first made for the Radial data with respect to the track defined by the Planars. The Radial track angle effect is then calibrated by fitting one free parameter which is subsequently fixed. In the final fit the Planar and Radial data are fitted simultaneously with free parameters $\Delta\alpha$, Δx, Δy and Δz for each of the three Radial chambers (Fig. 42), but with the Planar alignment parameters fixed. The results are shown in Table 8. None of the resulting corrections have a significant effect on the track reconstruction.

9. Performance

The performance of the reconstruction code has been assessed mainly by using a Monte Carlo simulation, with cross-checks from real data. The simulation will be briefly described, followed by the results of various measures of performance.

9.1. Simulation

The H1 simulation program uses the GEANT framework [17] to track particles through the detector. The GEANT description of the Forward Tracker treats each Planar drift cell as a single volume; for the Radials, each chamber is a single volume (i.e. the cathode planes are not included). The GEANT tracking code outputs a direction and momentum for each particle at the entrance and exit point of each volume. This is followed by a simulation of the digitisation process. A full simulation of the drift of charge in the chamber gas, followed by the response of the analogue electronics and the QT code, is impractical, so a parametrised simulation is used. This begins with the mean energy loss as a function of momentum and particle type. Landau fluctuations in the energy loss are simulated according to the GEANT routine GLANDZ. This energy is then scaled to give approximately the same average Q value as seen in real data. For the Radials, the charge is split according to the inverse of the charge division algorithm used in reconstruction (see Section 4.3.2) with equal preamplifier gains. Hits are removed using an efficiency derived from real data, but without including any correlations with the energy deposited (see Table 6). The limits on acceptance due to the Lorentz angle are included.

True random noise is very rare (around 1 hit per event). However, analysis of data shows that there is a significant background of track-related noise hits within a few millimetres of the true hits. These are simulated using parametrised distributions derived from data.

The detailed fluctuations in the FADC pulse shape are not currently well understood. Consequently, a standard (triangular) pulse is used as input to an emulation of the QT algorithm (Section 3), with various pulse-shape dependent effects added empirically. These include the two-track resolution, parametrised as a linear rise from 0% separation efficiency at 1 mm to 100% at 2.8 mm; the drift time of a group of hits when unresolved is taken as a charge-weighted average for the Planars and the time of the largest pulse for the Radials. The charge integral for the Radials is truncated at the start of the following hit if it is closer than the normal integration length.

The drift and charge measurements are then smeared using empirical resolutions, including the variation of drift resolution with drift distance (see Section 4). The smearing is increased if there is a close preceding hit, dependent on both the hit separation and the relative pulse heights. If the smeared charge is too small the hit is discarded. A linear distance-to-time relation is used, with a similar drift velocity to the average in real data.

The simulation described above gives a generally reasonable match with the data at the segment level. However, there is evidence for a correlated loss of hits in a

Table 8
Radial alignment parameters with the Planar alignment parameters fixed at the values given in Table 7, together with an estimate of the errors

Module	0	1	2	Error
$\Delta\alpha$ [mrad]	0.26	0.24	0.31	0.20
Δx [μm]	−192	166	−92	70
Δy [μm]	−376	−120	131	70
Δz [μm]	−309	405	269	500

Table 9
Probability of removing all hits from a given track in one drift cell for Radials (R) and Planars (P)

Supermodule	0	1	2
Probability (R)	0.05	0.05	0.25
Probability (P)	0.07	0.08	0.09

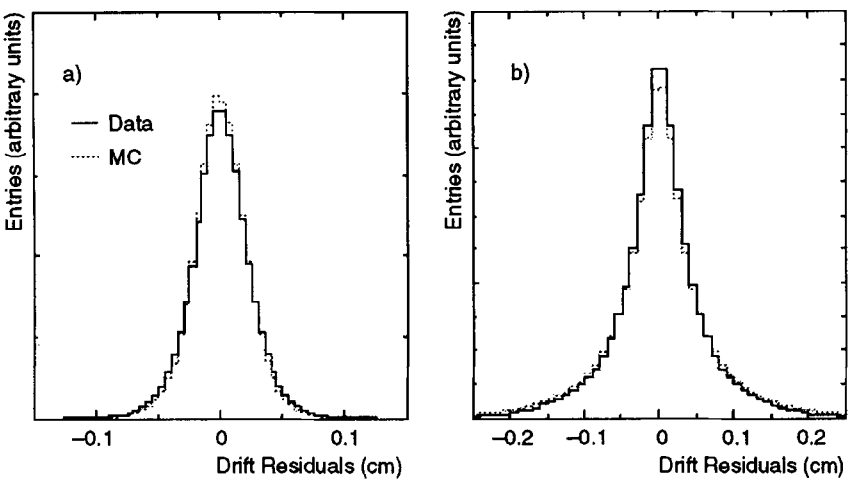

Fig. 43. Single segment drift residuals for both data and Monte Carlo for (a) Planars and (b) Radials.

drift cell at an appreciable rate, due either to timing problems, to breakdown or to other problems within the cell. This loss is estimated from the distribution (Table 10) of segments attached to individual tracks and is given in Table 9. The 25% loss in Radial Supermodule 2 can be attributed to the high hit density resulting from interactions in the collimator (Section 2).

9.2. Comparison between simulated and real data

Neutral current deep inelastic events have been generated by the LEPTO [18] program, and after simulation and reconstruction have been selected to have significant hadronic activity, a large proportion of which is in the FTD. The primary track multiplicity is ~10 to 15. In addition there are 40 to 60 mainly low momentum secondary tracks, a substantial number of which originate from the collimator and only penetrate the last Supermodule. The simulation used the efficiences for the 1993 data-taking period (Table 6).

The output of the simulation has been compared in detail with real data with the same selection, using measures which are insensitive to the underlying physics processes. The primary comparison is at the segment finding level; Fig. 43 shows the drift residuals for single segments for both simulated and real data. The agreement is good. The radius reconstruction depends on the details of charge fluctuations, which are not well understood and not well reproduced by the Monte Carlo, but the track reconstruction does not depend significantly on the radius measurement.

Fig. 44 shows the distributions of the numbers of hits on Planar and Radial segments, which indicate that the hit finding efficiency is approximately correct. The data distribution for the Radials is broader than the Monte Carlo due to summing over runs with differing efficiencies. Fig. 45 shows the χ^2 probability distribution for the overall

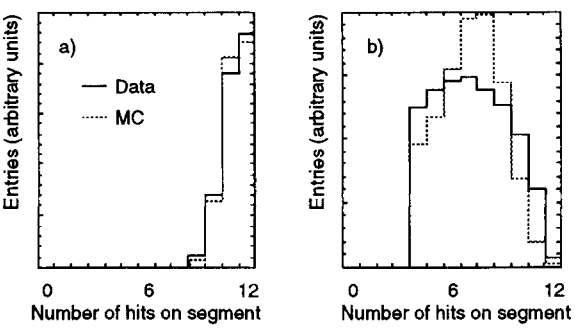

Fig. 44. Number of hits on single segments for both data and Monte Carlo for (a) Planars and (b) Radials.

track fit. Although the fraction of tracks in the low-probability bin is sensitive to pattern recognition errors, and in particular to the presence of track-related noise hits, the agreement between Monte Carlo and data is excellent.

Table 10 shows the distribution of the number of Planar

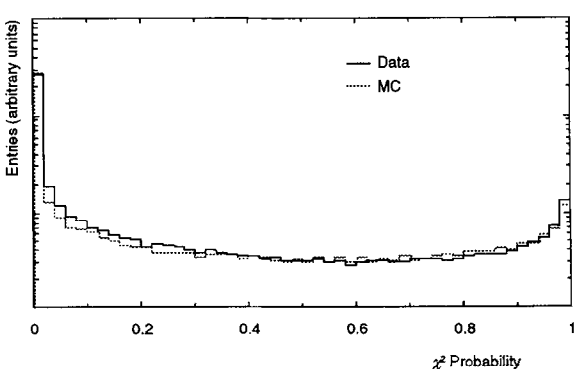

Fig. 45. χ^2 probability distribution for the overall track fit.

Table 10
The percentage of tracks in data (Monte Carlo) with different numbers of Radial (R) or Planar (P) segments attached. All tracks are required to have at least one Planar segment attached

	0 R	1 R	2 R	3 R	Any R
1 P	48.5 (35.2)	18.4 (23.1)	9.4 (12.4)	2.1 (2.5)	78.4 (73.2)
2 P	3.7 (4.2)	6.2 (8.5)	4.9 (7.0)	2.3 (2.3)	17.1 (22.0)
3 P	0.7 (0.7)	1.5 (1.8)	1.5 (1.7)	0.8 (0.6)	4.5 (4.8)
Any P	52.9 (40.1)	26.1 (33.4)	15.8 (21.1)	5.2 (5.4)	100.0 (100.0)

and Radial segments attached to tracks. The distributions are influenced by the underlying physics processes. Nevertheless there is good agreement between data and Monte Carlo, indicating that the hit and cell efficiencies are reasonably accurate, and that the resolutions lead to comparable segment linking efficiencies.

It can be seen from the above figures and tables that the simulation gives an excellent description of the real data at the hit, segment and track level. The simulation gives a sufficiently good match to allow reliable figures on reconstruction performance to be determined.

9.3. Performance

Important performance criteria are the track finding efficiency as a function of angle and momentum (particularly for primary tracks), and the momentum and angular resolution. These have been evaluated for neutral current events using the simulated data described above.

Fig. 46 shows the track finding efficiency as a function of pseudorapidity for primary tracks with momentum above 0.5 GeV/c. The dotted line shows the corresponding efficiency for the H1 Central Tracker. The comparison is with that Monte Carlo track which contributes the largest number of hits to the pattern recognised track. The variation of efficiency with angle is determined by the Forward Tracker acceptance, while the main limiting factor on the maximum efficiency is the correlated loss of all data in a drift cell (Table 9). The figure shows that the efficiency rises from 50% at 6° to 80% at 9°. The Tracker increases the range of track measurements in the forward direction by one unit of pseudorapidity.

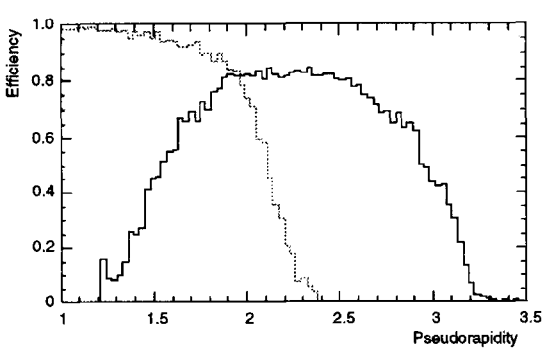

Fig. 46. Track finding efficiency as a function of pseudorapidity for primary tracks with momentum above 0.5 GeV/c. The dotted line shows the corresponding efficiency for the H1 Central Tracker.

Fig. 47 shows the efficiency as a function of momentum, p, for primary tracks with $9° < \theta < 18°$ (which is the range over which the efficiency is independent of θ). It can be seen that the efficiency is essentially independent of momentum above 0.5 GeV/c.

The fraction of tracks found more than once, i.e. split into more than one piece, is less than 1%, and is roughly independent of angle and momentum. For 70% of reconstructed tracks the fraction of hits which are correct is greater than 80%.

Another way of assessing the track finding efficiency is to look at events with tracks in other tracking detectors, and scan by eye to see whether corresponding tracks are seen in the Forward Tracker. This has been done for samples of a few hundred events, for low track multiplicities, and in a limited angular range. It gives results in agreement with those from Monte Carlo data.

Fig. 48 shows the distributions of $\Delta(q/p)$, the difference between the reconstructed and true q/p, for tracks with and without a fit to the primary interaction vertex. In each case the distributions are shown for $0.5 < p < 1$ GeV/c, $1 < p < 3$ GeV/c and $p > 3$ GeV/c. Table 11 gives the resolutions in q/p from the fits shown in Fig. 48 [19]. The momentum dependence is due to multiple scattering. It can be seen that the inclusion of the vertex improves the momentum resolution by about a factor of 2 for momenta above 3 GeV/c. The polar angular resolution is 0.2 mrad for

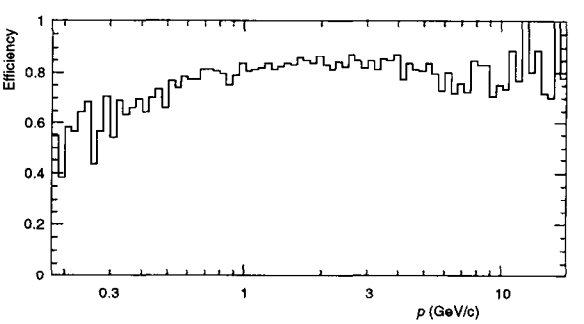

Fig. 47. Efficiency as a function of p for primary tracks with $9° < \theta < 18°$.

Table 11
Resolution in q/p (%/GeV/c) for the FTD

Momentum range	$0.5 < p < 1$ GeV/c	$1 < p < 3$ GeV/c	$p > 3$ GeV/c
Tracks without vertex	19.9	7.9	5.4
Tracks with vertex	14.1	5.6	2.7

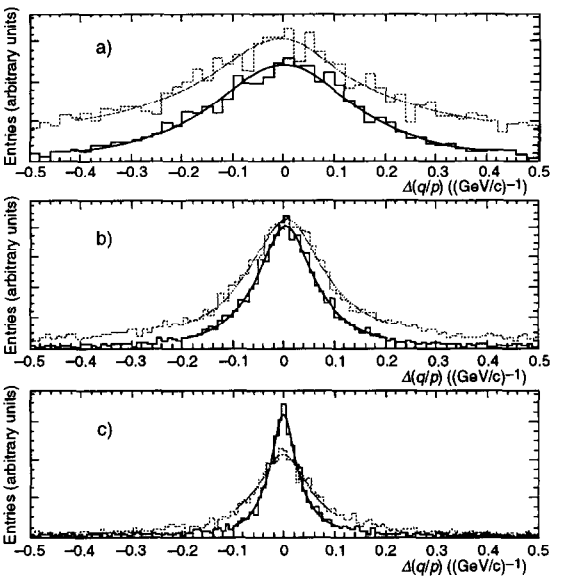

Fig. 48. $\Delta(q/p)$ for tracks with and without a fit to the primary vertex for (a) $0.5 < p < 1$ GeV/c, (b) $1 < p < 3$ GeV/c and (c) $p > 3$ GeV/c. The solid histograms are for primary tracks with a vertex fit, the dashed for all tracks, but without a vertex fit. The fitted curves are generalised Breit–Wigners [19].

three-module, high momentum tracks and better than 1 mrad for the majority of tracks.

10. Summary

This paper has described the reconstruction of tracks in a detector that operates in an environment made complex by the high hit density from proton fragmentation, and the large number of photon conversions and other secondary interactions in the end wall of the Central Tracker and the nearby collimator.

The procedures used to analyse the FADC pulses and determine the drift velocities, timing offsets, resolutions and efficiencies of the chambers have been discussed. A technique has been developed for alignment of the multi-detector system.

The pattern recognition and track fitting procedures that have been optimised for the mix of Radial and Planar chambers of the H1 Forward Track Detector have been described in detail. Monte Carlo studies, supplemented by visual scanning, have shown that in spite of the complexity of the events, tracks are found with an efficiency ~80% over a wide range of the acceptance. The Tracker extends the range of track measurement in the forward direction by one unit of pseudorapidity.

Acknowledgements

We wish to thank the staff at the UK Universities and RAL, who have been responsible for the design, construction and maintenance of the FTD, and whose efforts have provided the foundation for the work described in this paper. The hospitality extended to us by the staff and directorate at DESY, leading up to and during the first years of HERA operation, has been greatly appreciated. We thank the funding agencies for their support and the H1 experiment and the UK PPARC (formerly SERC), in particular, for financial support of the FTD project. We also wish to thank the staff of the Cosener's House for their excellent hospitality which provided an environment that greatly facilitated the writing of this paper. Finally our thanks for carcful typing and constructively critical reading of this paper go respectively to Miss Ann Richardson of the Rutherford Appleton Laboratory and to Dr. David Newton of the University of Lancaster.

References

[1] W. Buchmüller and G. Ingelman (eds.), Proc. Workshop on Physics at HERA, DESY, vol. 1, October 29–30, 1991.
[2] The H1 Detector at HERA, H1 Collaboration, DESY 93-103 (July 1993).
[3] Technical Proposal for the H1 Detector, H1 Collaboration, DESY (March 1986).
[4] The techniques used in electron identification are described in more detail in H. Grässler et al., Nucl. Instr. and Meth. A 323 (1992) 401.
[5] The most detailed (although not necessarily up-to-date) description of the Forward Tracker may be found in The H1 Forward Tracker Description and Status, H1 FTD Group, DESY H1-TR-205 (October 1987).
[6] See for example G.A. Beck et al., Nucl. Instr. and Meth. A 283 (1989) 471;
H. Grässler et al., Nucl. Instr. and Meth. A 283 (1989) 622;
H. Grässler et al., Nucl. Instr. and Meth. A 310 (1991) 535;
J.M. Bailey et al., Nucl. Instr. and Meth. A 323 (1992) 184.
[7] D. Schaile, O. Schaile and J. Schwarz, Nucl. Instr. and Meth. A 242 (1986) 247.
[8] S.M. Tkaczyk et al., Nucl. Instr. and Meth. A 270 (1988) 373.

[9] D.P.C. Sankey, Ph.D. thesis, University of Liverpool, RALT-115, 1990.
[10] V. Radeka and P. Rehak, IEEE Trans. Nucl. Sci. NS-26 (1979) 225.
[11] F. Sauli, CERN 77-09 (1977).
[12] J.V. Morris, RAL report, to be published.
[13] R. Veenhof, CERN User Guide W5050, URL ⟨http://consult.cern.ch/writeup/garfield/main.html⟩.
[14] R. Früwirth, Nucl. Instr. and Meth. A 262 (1987) 447.
[15] V. Blobel, private communication.
[16] R. Früwirth, HEPHY-PUB 516/88, Vienna (1988);
R. Früwirth et al., HEPHY-PUB 578/93, Vienna (1993).
[17] CERN Program Library Q123, URL ⟨http://wwwcn.cern.ch/asdoc/geant/GEANTMAIN.html⟩.
[18] G. Ingelman, Proc. Workshop on Physics at HERA, eds. W. Buchmüller and G. Ingelman, DESY, Vol. 3, October 29–30, 1991, p. 1366.
[19] We define the generalised Breit–Wigner distribution as

$$G(x) = \alpha\left(1 + [2^{1/\beta} - 1]\left(\frac{x - \bar{x}}{\gamma}\right)^2\right)^{-\beta}.$$

The function has half-width at half height equal to γ and approaches a simple Breit–Wigner as β approaches 1 or a Gaussian as it tends to infinity. The values in Table 11 are $\gamma(2 \ln 2)^{-1/2}$, which corresponds to σ for a Gaussian.